Internal tides off the Amazon shelf Part I: importance for the structuring of ocean temperature during two contrasted seasons

Fernand Assene [1], Ariane Koch-Larrouy [2], Isabelle Dadou [3], Michel Tchilibou [4], Guillaume Morvan [5], Jérôme Chanut [6], Vincent Vantrepotte [7], Damien Allain [8], Trung-Kien Tran [9].

[1,2,3,5,8] Université de Toulouse, LEGOS (CNRS/IRD/UPS/CNES), Toulouse, France, [1,6] Mercator Ocean International, 31400 Toulouse, France, [4] Collecte Localisation Satellites (CLS), 31500 Ramonville Saint-Agne, France, [7,9] Laboratoire d'Océanologie et de Géosciences (LOG), 62930 Wiméreux, France

Correspondence to: Fernand Assene (assene@legos.obs-mip.fr)

Abstract

Tides and internal tides (IT) in the ocean can significantly affect local to regional ocean temperature, including sea surface temperature (SST), via physical processes such as diffusion (vertical mixing) and advection (vertical and horizontal) of water masses. Offshore of the Amazon River, strong IT have been detected by satellite observations and well modelled; however, their impact on temperature, SST and the identification of the associated processes have not been studied so far. In this work, we use high-resolution (1/36°) numerical simulations with and without the tides from an ocean circulation model (NEMO). This model explicitly resolves the internal tides (IT) and is therefore suitable to assess how they can affect ocean temperature in the studied area. We distinguish the analysis for two contrasted seasons, from April to June (AMJ) and from August to October (ASO), since the seasonal stratification off the Amazon River modulates the IT's response and their influence in temperature.

The generation and the propagation of the IT in the model are in good agreement with observations. The SST reproduced by the simulation including tides is in better agreement with satellite SST data compared to the simulation without tides. During ASO season, stronger meso-scale currents, deeper and weaker pycnocline are observed in contrast to the AMJ season. The observed coastal upwelling during ASO season is better reproduced by the model including tides, whereas the no-tide simulation is too warm by +0.3 °C for the SST. In the subsurface above the thermocline, the tide simulation is cooler by -1.2 °C, and warmer below the thermocline by +1.2 °C compared to the simulation without the tides. The IT induce vertical mixing on their generation site along the shelf break and on their propagation pathways towards the open ocean. This process mainly explains the cooler temperature at the ocean surface and is combined with vertical and horizontal advection to explain the cooling in the subsurface

33 water above the thermocline and a warming in the deeper layers below the thermocline. The

34 surface cooling induced in turn an increase of the net heat flux from the atmosphere to the

35 ocean surface, which could induce significant changes in the local and even for the regional

36 tropical Atlantic atmospheric circulation and precipitation.

37   We therefore demonstrate that IT, via vertical mixing and advection along their

38 propagation pathways, and tides over the continental shelf, can play a role on the temperature

39 structure off the Amazon River mouth, particularly in the coastal cooling enhanced by the IT.

40 **Keywords**: internal tides, Amazon continental shelf and slope, temperature, modeling, satellite

41 data, mixing, heat flux.

I.   Introduction

43   Temperature and its spatial structure play a crucial role in ocean dynamics, including

44 water mass formation (Swift and Aagaard, 1981; Lascaratos 1993; Speer et al. 1995), transport

45 and mixing of other tracers in the ocean and exchanges with other biosphere compartments

46 (Archer et al. 2004, Rosenthal et al. 1997), and most importantly on surface heat exchange at

47 the interface with the atmosphere (Calyson and Bagdanoff, 2013; Mei et al. 2015) and can thus

48 significantly influence the climate (Li et al. 2006; Collins et al. 2010). This oceanic thermal

49 structure can be modified at various spatial and temporal scales by different processes external

50 to the ocean such as incident solar radiation, heat fluxes with the atmosphere, winds,

51 precipitation and freshwater inputs from rivers. Processes internal to the ocean also play a

52 crucial role in this thermal structure, such as mass transport by currents and eddies (e.g.:

53 Aguedjou et al., 2021), mixing by turbulent diffusion (Kunze et al. 2012), tides and internal

54 tidal waves (IT) (Barton et al., 2001; Smith et al., 2016; Salamena et al., 2021). The role of IT

55 on the thermal structure of the ocean is of increasing interest with many studies in recent years,

56 but remains poorly understood in many ocean regions, and especially off the Amazon shelf.

57   In a stratified ocean, the passage of a barotropic tide over a topographic profile with a

58 steep slope (continental slope, seamount, oceanic ridge) generates a disturbance in the flow

59 that gives rise to a so-called baroclinic tide, with the same frequency, but with higher vertical

60 velocities (Zhao et al., 2016). The baroclinic tide, also known as internal tidal waves (IT), thus

61 captures part of the energy of the barotropic tide, propagates it and dissipates it into the global

62 ocean by diapycnal mixing (Zhao et al., 2012), i.e., up to about 1 TW in the deep ocean (Egbert

63 and Ray, 2000; Niwa and Hibiya, 2011) and thus helps to feed the thermohaline circulation

64 (Munk and Wunsch, 1998). These two tidal processes (barotropic tide and IT) thus bring

65   together a set of mechanisms for transferring and redistributing energy from larger to smaller

66   oceanic scales, which can be understood as a tidal energy cascade. The dissipation of IT occurs

67   mainly locally at the generation sites for high-mode IT that are associated with higher vertical

68   shear, while a significant part of the energy dissipates offshore along their propagation path for

69   low-mode IT (Zhao et al., 2016). Results from models in the Indonesian seas (Koch-Larrouy

70   et al., 2007 and Nugroho et al., 2018) and observations in the Celtic Sea (Sharples et al. 2007)

71   and the Yellow Sea (Xu et al., 2020), point out that IT dissipate most of their energy vertically,

72   where the vertical gradient of stratification is maximal in the water column. IT can also

73   vertically advect water masses during their propagation. They thus induce vertical

74   displacements of the isopycnal levels of several meters to a few tens of meters, observable in

75   the thermocline (Wallace et al., 2008; Xu et al. 2020). Denmann and Garett (1983) and Bordois

76   et al. (2016) point out that the stratification peak acts as a waveguide for the propagation of IT.

77   The mixing and advection induced by IT results in a change in temperature structure

78   throughout the water column. In surface waters, Smith et al. (2016) report that IT can induce

79   surface cooling varying between 1 °C and 5 °C depending on the ocean region. Koch-Larrouy

80   et al. (2007) and Nagai and Hibiya (2015) have shown, for the Indonesian region, that IT

81   induces a surface cooling of -0.5 °C on average and that this decreases cloud convection in the

82   atmosphere on a local scale, which in turn reduces precipitation by 20% and thus plays an

83   important role on the climate on a regional scale. Furthermore, Jithin and Francis (2020)

84   showed that IT can also affect the temperature in deep waters (> 1600 m), leading to a warming

85   of the order of 1–2 °C.

86   The barotropic tides dissipate most of their energy in shallow coastal waters by bottom

87   friction when the mean ocean depth becomes less than the amplitude of the tide (Lambeck and

88   Runcorn, 1977; Le Provost and Lyard, 1997), and can thus modify temperature. Furthermore,

89   Gonzalez-Haro et al. (2019) showed that barotropic and baroclinic tidal currents can induce

90   temperature fluctuations by horizontal advection of surface water masses over hundreds of

91   kilometers, and thus contribute to modifying the SST. These two tidal processes (barotropic

92   and baroclinic) can also affect other tracers such as nutrients, chlorophyll and sediments

93   (Heathershaw et al., 1987; da Silva et al., 2002; Sharples et al., 2007; Pomar et al., 2012;

94   Muacho et al., 2014; Tuarena et al., 2016; Barbot et al., 2022).

95   Our study focuses on the oceanic region of northern Brazil off the Amazon River, where

96   IT have been highlighted in previous studies, but their impact on the thermal structure is not

97   currently known. This region is characterized by a broad, shallow continental shelf at the mouth

98   of the Amazon River ended by a steep slope, i.e., a bathymetry variation of 200-2000 m over

99   some tens of kilometers (Fig.1). Along this slope, six sites (A to F) of IT generation have been

100 identified (Fig.1), the most intense of which (A and B) are in the south of the region (Magalhaes

101 et al. 2016, Barbot et al. 2021 and Tchilibou et al. 2022). A strong seasonal coastal current, the

102 Brazilian North Current (NBC), strongly influences the study area and flows along the coast

103 from the southeast to the northwest (Johns et al., 1990).

104   This region shows a seasonal variation in the position of the winds and the Intertropical

105 Convergence Zone (ITCZ) during the year, which directly influences the discharge of the

106 Amazon River, the oceanic circulation (Xie and Carton, 2004), and therefore the stratification.

107 This impacts the activity of internal tidal waves (Barbot et al., 2021). Two seasons can be

108 clearly distinguished by their properties on water masses and currents.

109   The first season runs from March to July, during this time the ITCZ is in its most

110 equatorial position and lies in the heart of our region. The increase in rainfall over the ocean

111 leads to a colder and more homogeneous SST far from the coast. The discharge of the Amazon

112 River into the ocean reaches its peak ($> 3\times10^5$ m³.s⁻¹) and the surface temperature in the coastal

113 zone, although homogeneous, is warmer than offshore. At the end of this season, driven by the

114 strong river discharge, the Amazon plume along the shelf extends beyond 8°N, and sometimes

115 into the Caribbean region (Müller-Karger et al., 1989; Johns et al., 1998). The stratification is

116 somewhat stronger and more homogeneous horizontally, and the maximum of its vertical

117 gradient (pycnocline) is closer to the surface. This latter point leads to a stronger conversion of

118 energy from barotropic to baroclinic, and a stronger local (first 50 km) dissipation of internal

119 tidal wave energy (Barbot et al., 2021; Tchilibou et al., 2022). NBC and eddy kinetic energy

120 (EKE) are weak in the region (Aguedjou et al., 2019). Close to the equator, the NBC develops

121 a retroflection towards 1°N latitude that feeds the Equatorial Under-Current (EUC) transporting

122 water masses eastwards to the Gulf of Guinea (Didden and Schott, 1993, Dimoune at al., 2022).

123   Contrasting with this first season, due to different oceanic and atmospheric conditions,

124 the second season extends from August to December. During this season, the ITCZ migrates

125 to its northernmost position around 10°N. In response, rainfall in this area decreases and the

126 Amazon River discharge also decreases to its minimum ($\sim 10^5$ m³.s⁻¹), the extension of the river

127 plume is therefore reduced to no more than 200–300 km offshore from the mouth of the

128 Amazon between November and December (Johns et al., 1998, Garzoli et al., 2003). During

129 this season, cold water (< 27.6 °C) associated with the western extension of the Atlantic cold-

130 water tongue (ACT) enters the region from the south and runs along the edge of the continental

131   shelf to about 3°N (Lentz and Limeburner, 1995; Neto et al., 2014), forming a cold cell often

132   referenced as a seasonal upwelling. The stratification of the study area is strongly modified

133   compared to the previous season. The pycnocline becomes somewhat deeper. The generation

134   of IT on the slope and their local dissipation are weaker compared to the first season (Barbot

135   et al., 2021; Tchilibou et al., 2022). Currents and eddy activity become stronger. The NBC

136   becomes stronger, farther from the coast and deeper, it develops a retroflection (NBCR)

137   between 5°–8° N that feeds the North Equatorial Counter-Current (NECC) transporting the

138   water masses towards the east of the tropical Atlantic. This generates very large anticyclonic

139   eddies (NBC Rings) exceeding 450 km in diameter (Didden and Schott, 1993; Richardson et

140   al., 1994; Garzoli et al., 2004), which in turn transport water masses towards the Northern

141   Hemisphere (Bourlès et al., 1999a; Johns et al., 1998; Schott et al., 2003). In addition, there are

142   more cyclonic/anticyclonic eddies from the Gulf of Guinea during this season. All this

143   contributes to the strengthening of the EKE, which reaches its maximum in this season

144   (Aguedjou et al., 2019). When the baroclinic tidal flow interacts with the general circulation,

145   it is deviated from its trajectory, thus we have a so-called incoherent baroclinic tide (Buijsman

146   et al., 2017). This IT-circulation interaction is thus reinforced during this second season

147   because of the more intensified currents and eddy activity (Tchilibou et al., 2022).

148   On the Brazilian continental shelf, Geyer et al. (1996) suggests the presence of internal

149   tidal waves from current data. Later, Lentini et al. (2016) based on SAR imagery, shows small-

150   wavelength (~ 10 km) internal solitary waves (ISW) packets propagating along and across the

151   continental shelf, and generated by linear non-hydrostatic interactions between the NBC and

152   barotropic tidal currents. Using a model, Molinas et al. (2020) show that baroclinic tidal

153   currents play an important role on sediment transport on this continental shelf. On a global

154   scale, several studies from altimetry observations (Zhao et al., 2012, 2016; Zaron et al., 2017,

155   2019) or models (Munk and Wunsch, 1998; Shriver et al., 2012; Arbic et al., 2012; Niwa and

156   Hibiya, 2011, 2014; Buijsman et al. 2016) have shown intense activity of IT along the steep

157   slope of the continental shelf. At the surface, using SAR imagery, Jackson (2007) and

158   Magalhaes et al. (2016) describe longer wavelength ISW (~ 50–150 km) that propagate

159   offshore from the slope. The latter emphasizes the modulation of their propagation by the

160   seasonal variation of the NECC, and from a model, establishes that these ISW originate from

161   instabilities and energy loss of IT coming from the slope, mainly at sites A and B. Recently, de

162   Macedo et al. (2023) provided a somewhat more comprehensive description of the seasonal

163   characteristics of these ISW, with the predominant origin remaining at sites A and B. Barbot

164   et al. (2021) focused on the influence of stratification on the IT generation on the shelf as well

165   as their propagation offshore. Finally, also in seasonal scale, Tchilibou et al. (2022) looked at

166   the variation of the energy associated with IT from their generation to their dissipation, as well

167   as the interaction of these waves with the general circulation. However, the interactions

168   between IT and tracers such as temperature, salinity or chlorophyll have not received much

169   interest from the scientific community in this region.

170   Hydrodynamic and biogeochemical conditions on the shelf and off the mouth of the

171   Amazon were studied during the AMASSEDS campaigns in the early 1990s (DeMaster and

172   Pope, 1996; Nittouer and DeMaster, 1996) and the various "*Camadas Finas*" campaigns

173   (Araujo et al., 2017, 2021). Furthermore, using data from the two REVIZEE campaigns and

174   TMI-SST satellite data, Neto et al. (2014) studied the seasonal cooling of surface waters, which

175   occurs between the months of July and December. They conclude that the NBC is responsible

176   for the upwelling of cold-water masses ($< 27.5 \,°C$) to the more superficial layers. Subsequently,

177   Araujo et al. (2016), using in addition a realistic model, suggest that the tide would have a key

178   role to play in intensifying this cooling. Indeed, through twin simulations with and without tides,

179   they show that with tide there is a $-0.3 \,°C$ cooling of the surface temperature. These analyses

180   remain qualitative and do not allow determining what are the processes at work. Knowing that

181   we are in an area with a strong activity of internal tidal waves, the question remains whether

182   and by what processes these IT can structure the temperature both at the surface and inside the

183   water column.

184   In order to answer the above questions, we used a high-resolution model ($1/36°$) and a

185   satellite SST product, with the aim of highlighting the impact of IT on the temperature structure

186   and associated processes. These observations, our modeling, as well as the methods used are

187   described in section II. The validation of some barotropic and baroclinic tide's characteristics

188   as well as SST are present in section III. The impacts of IT on the temperature structure, the

189   influence on heat exchange at the interface between the atmosphere and the ocean, and finally

190   the processes involved, are analyzed in section IV. Summary and discussions of the obtained

191   results are presented in a last section.

192

193   **II.   Data and Methods**

194   **II.1. Satellite Data used: TMI SST**

195   This dataset derived from Tropical Rainfall Measurement Mission (TRMM), which

196   performs measurements using onboard TRMM Microwave Imager (TMI). The microwaves

197 can penetrate clouds and are therefore very important for data acquisition in low latitude

198 regions, cloudy covered during long periods of raining seasons. We use Remote Sensing

199 Systems (RSS) TMI data products v7.1, which is the latest version of TMI SST. It contains a

200 daily mean of SST with a 0.25°×0.25° grid resolution (~ 25 km). This SST is obtained by inter-

201 calibration of TMI data with other microwave radiometers. The TMI SST fully description and

202 inter-calibration algorithm is detailed in Wentz et al. (2015).

II.2. Model: *AMAZON36* configuration

204 The numerical model used in this study is the Nucleus for European Modelling of the

205 Ocean (NEMOv4.0.2, Madec et al., 2019). The "*AMAZON36*" model configuration covers the

206 western tropical Atlantic region with a 1/36° horizontal grid, from the Amazon River mouth to

207 the open ocean. Several configurations with same grid resolution, but for the former

208 NEMOv3.6 (Madec, 2014), exists for the same region, but either includes Caribbean Sea

209 (Hernandez et al., 2016), or are not far extended to the east even used for tides study (Ruault

210 et al., 2020). The present configuration is wider to capture, on their pathways, all the internal

211 tide generating from the Brazilian shelf. Hence, the domain lies between 54.7°W–35.3°W and

212 5.5°S–10°N (Fig.1). In contrast with former configurations, we do not use multiple nested grids

213 here, but a single grid. The vertical grid comprises 75 vertically fixed z-coordinates levels, finer

214 grid refinement close to the surface with 23 levels in the 100 m, and cell thickness reaching

215 160 m when approaching the bottom. Both horizontal and vertical grid resolutions are therefore

216 acceptable to resolve low-mode internal tides and were already used for that purpose (Tchilibou

217 et al., 2022).

218 A third order upstream biased scheme (UP3) with built-in diffusion is used for

219 momentum advection, while tracer advection relies on a 2nd order Flux Corrected Transport

220 (FCT) scheme. A Laplacian isopycnal diffusion with a constant coefficient of 20 m².s⁻¹ is used

221 for tracers. The temporal integration is achieved thanks to a leapfrog scheme combined with

222 an Asselin filter to damp numerical modes (baroclinic time step is 150 s). The $k-\varepsilon$ turbulent

223 closure scheme is used for the vertical diffusion coefficients. Bottom friction is quadratic with

224 a bottom drag coefficient of 2.5×10⁻³, while lateral wall free-slip boundary conditions are

225 assumed. A time splitting technique is used to resolve the free surface, with the barotropic part

226 of the dynamical equations integrated explicitly.

227 We use the General Bathymetric Chart of the Oceans (GEBCO, 2020) interpolated onto

228 the model horizontal grid, with the minimal depth equal to 12.8 m. The ocean model is forced

229 by the ERA-5 atmospheric reanalysis (Hersbach et al., 2020). The river discharges are based

230   on monthly means from hydrology simulation of ISBA model (Interaction Sol-Biosphère-

231   Atmosphère, see description in ISBA - National Centre for Meteorological Research), and are

232   prescribed as surface mass sources with null salinity, and we use a multiplicative factor of 90%

233   based on a comparison with the HYBAM interannual timeseries (HYBAM, 2018). The model

234   is forced at its open boundaries by the fifteen major high-frequency tidal constituents (M2, S2,

235   N2, K2, 2N2, MU2, NU2, L2, T2, K1, O1, Q1, P1, S1, and M4) and barotropic currents derived

236   from FES2014 atlas (Lyard et al., 2021). At the open boundaries, we prescribe MERCATOR-

237   GLORYS12 v1 (Lellouche et al., 2018) for temperature, salinity, sea level, current velocity and

238   derived baroclinic velocity.

239   The simulation was initialized on the 1st of January 2005, and ran for 10 years until

240   2015. In this study, we use model outputs from 2013 to 2015. Indeed, the model has reached

241   an equilibrium in terms of seasonal cycle after 2 years (2005-2006) of run. The same model

242   configuration without the tides is used to highlight the influence of tides and IT on the

243   temperature structure. To assess the realism of the model, we perform validation of various

244   state variables used in this study such as the current's circulation, temperature, salinity,

245   stratification as well as the barotropic and baroclinic tide properties.

246   **II.3. Methods**

247   **II.3.1. Barotropic/baroclinic tide separation and tide energy budget**

248   We follow Kelly et al. (2010) method to separate barotropic and baroclinic tide

249   constituents: pressure, currents and energy flux. No modal separation is done, then tidal

250   constituents obtained encompass the energy of all propagation's modes. Note that the

251   barotropic/baroclinic tide separation is performed directly by the model for better accuracy,

252   however, by this way it has the disadvantage of being very costly in terms of computing time.

253   We therefore analyze only for one year (2015) the M2 frequency, since M2 is the major tidal

254   constituent in this region, representing $\sim$ 70% of the tidal energy (Beardsley et al., 1995;

255   Gabioux et al., 2005 and Tchilibou et al., 2022).

256   The barotropic and baroclinic tide energy budget equations are obtained by ignoring as

257   the first-order approximation the energy tendency, the nonlinear advection and the forcing

258   terms (Wang et al., 2016). Then, the remaining equations are reduced to the balance between

259   the divergence of the energy flux, the dissipation and the energy conversion from barotropic to

260   baroclinic (Buijsman et al., 2017; Tchilibou et al., 2018, 2020, 2022; Jithin and Francis, 2020

261   ; Peng et al., 2021) :

262    $$D_{bt} + \nabla_h \cdot F_{bt} + CVR \approx 0 \qquad (\text{W.m}^{-2}), \qquad (1)$$

263
$$D_{bc} + \nabla_h \cdot F_{bc} - CVR \approx 0 \qquad (\text{W.m}^{-2}), \qquad (2)$$

264   bt and bc indicate the barotropic and baroclinic terms, D is the depth-integrated energy

265   dissipation, which can be understood as a proxy of the real dissipation since D may encompass

266   the energy loss of other tidal harmonics, non-linear terms and/or numerical dissipation (see

267   Nugruho et al., 2018), $\nabla_h \cdot F$ represents the divergence of the depth-integrated energy flux,

268   whilst CVR is the depth-integrated barotropic-to-baroclinic energy conversion, i.e. the amount

269   of incoming barotropic energy which is converted into internal tides energy over the steep

270   topography, with :

271
$$CVR = \langle \nabla H \cdot U_{bt}^* P_{bc}^* \rangle \qquad (\text{W.m}^{-2}), \qquad (3)$$

272
$$F_{bt} = \int_H^\eta \langle U_{bt} P_{bt} \rangle \, d_z \qquad (\text{W.m}^{-1}), \qquad (4)$$

273
$$F_{bc} = \int_H^\eta \langle U_{bc} P_{bc} \rangle \, d_z \qquad (\text{W.m}^{-1}), \qquad (5)$$

274   where the angle bracket denotes the average over tidal period, ∇H is the slope of the bathymetry,

275   U_{bt}^* is the barotropic current and P_{bc}^* is the baroclinic pressure perturbation both at the bottom,

276   H is the bottom depth, η the surface elevation, $U(u, v)$ is the horizontal velocity, P is the

277   pressure, then F is the energy flux and allows the propagation pathways of the given tide to be

278   highlighted.

279 **II.3.2. 3-D heat budget equation for temperature**

280   The three-dimensional temperature budget was computed online and further analyzed.

281   It is the balance between the total temperature trend and the sum of the temperature advection,

282   diffusion and solar radiative and non-solar radiative fluxes (e.g.: Jouanno et al., 2011;

283   Hernandez at al., 2017):

284
$$\partial_t T = \underbrace{-u\partial_x T - v\partial_y T - w\partial_z T}_{ADV} \; \underbrace{- \partial_z (Kz \partial_z T)}_{ZDF} + LDF_T + FOR_Z + Numdiff \qquad (°C.s^{-1}), \qquad (6)$$

285

286   Where T is the model potential temperature, [u, v, w] are the ~~space dimensional~~ velocity

287   components, ADV is the 3-D temperature advection (left to right: zonal, meridional and vertical

288   terms), ZDF is the vertical diffusion, LDF_T is the lateral diffusion, FOR_z is the tendency of

289   temperature due to penetrative solar radiation and has a vertical decaying structure. At the air-

290   sea interface, the temperature flux is equal to the non-solar heat flux (sum of the latent, sensible

291   and net infrared fluxes). FOR_z can modify temperature in the thin surface layer but will not be

292 shown in the following. *Numdiff* corresponds to ~~the sum of~~ the numerical diffusion for the

293 temperature. In this study, we assume that this last term is of second order and is not highlighted

294 here.

II.3.3. The atmosphere–ocean net heat flux

296 The atmosphere–ocean net heat flux (Qt) reflects the balance of incoming and outgoing

297 heat fluxes across the atmosphere-ocean interface (e.g.: Moisan and Niiler, 1998; Jayakrishnan

298 and Babu, 2013), it is defined as follows:

299 $$Q_t = Q_{SW} \pm Q_{LW} \pm Q_{SH} \pm Q_{LH} \qquad\qquad W.m^{-2}, \qquad (7)$$

300 with from left to right: the incident solar radiative flux (Q_{SW}), the net infrared radiative flux

301 (Q_{LW}), the incoming/outgoing sensible heat flux (Q_{SH}) which depends on the temperature

302 difference between the atmosphere and the ocean surface, and the incoming/outgoing latent

303 heat flux (Q_{LH}) which depends on the specific humidity difference between the atmosphere and

304 the ocean surface. All these four components of ~~the~~ Qt influence the variation of the ocean

305 surface temperature (SST). The last two components (Q_{SH} and Q_{LH}) have in addition a direct

306 dependence relationship with the SST. Since IT can change the SST, we are therefore interested

307 in knowing how it affects the net heat flux at the atmosphere-ocean interface.

III. Model validation

309 In this subsection we present for the M2 harmonic the barotropic and baroclinic tidal

310 characteristics of the model for the year 2015, and the SST for the whole period from 2013 to

311 2015, and we verify that they agree with the different observations.

III.1. M2 Tides in the model

313 The barotropic SSH (Fig.2b) of the model is compared with FES2014 (Lyard et al.

314 2021) (Fig.2a), *and* there is good agreement in terms of both amplitude and phase. Nevertheless,

315 near the coast, some differences are observed in terms of amplitude. The SSH of the model is

316 lower (~ +50 m) north of the mouth of the Amazon. However, inland and on the southern part

317 of the mouth, the model overestimates the amplitude (~ +20 m and ~ +40 m respectively). This

318 is in terms of order of magnitude like the biases in the Ruault et al. (2020) configuration that

319 they compared to the FES2012 product (Carrère et al., 2012) over the same region. Along the

320 steep slope of the bathymetry (see Fig.1), a portion of the incident barotropic tidal energy (black

321 arrows Fig.2c and Fig.2d, for FES2014 and the model, respectively) in the presence of

322 stratification is converted to baroclinic tidal energy. We compared the depth-integrated

Display figures in order of reference.

2a, 2b, ...

323   barotropic-to-baroclinic energy conversion rate (CVR) between the model (Fig.2d) and

324   FES2014 (Fig.2c). The model does reproduce the same conversion patterns of FES2014 but

325   can underestimate the CVR by about 30%. The bathymetry resolution plays a critical role in

326   CVR (Niwa and Hibiya, 2011), then the difference in bathymetry resolution between the model

327   (~ 3 km) and FES2014 (~ 1.5 km) could therefore explains that difference in CVR.

328   The critical slope for the M2 harmonic on the slope is greater than 1.2 (not shown),

329   consequently, the baroclinic tides (internal tidal waves) thus generated will therefore propagate

330   in the opposite direction to the barotropic tides, i.e., from the slope to the open ocean. The

331   baroclinic tidal flux of the model (black arrows in Fig.2e) highlights the existence of six main

332   sites of IT generation on the continental slope, two of which are more important (A and B), as

333   shown by Maghalaes et al. (2016), Barbot et al. (2021) and Tchilibou et al. (2022). From these

334   two main sites, the flow propagates offshore for nearly 1000 km. On its propagation path, the

335   baroclinic tide signs at the surface in SSH. We compared this signature for the model (Fig.2h)

336   with an estimate deduced from the altimeter tracks, produced by Zaron et al. (2019) (Fig.2g).

337   The model is in good agreement with the altimetry observations, with an overestimation of the

338   order of ~ +1.5 cm on the SSH maxima. It is important to note that the baroclinic SSH of the

339   model is an average over the year 2015, whilst the observations are an average over about 20

340   years. This longer period may smooth the amplitude of the signal obtained from the altimetry

341   observations. Also, the variability contained in the two averages is not the same, and this may

342   explain some differences in the positioning and amplitude of the maxima.

343   Figure 2f shows the full depth-integrated internal tidal energy dissipation for the model.

344   The estimated local dissipation of this energy is defined as follows:

345    $$P = (D_{bc} / CVR) * 100 \tag{8}$$

346   The local dissipation is then integrated at the embankment level in boxes A1, A2 and B

347   (Fig.2f, see coordinates in Table-2 in Tchilibou et al. 2022) and provides information that a

348   significant part of the energy is dissipated locally in the different boxes, i.e., about 30% (not

349   shown). The local dissipation at the generation sites is thus in good agreement with Tchilibou

350   et al. (2022). The remaining energy is exported offshore and dissipates along the propagation

351   path. This dissipation is more extensive offshore along path A, ~ 500 km from the slope, with

352   two patterns spaced approximately 120 km apart corresponding to propagation mode-1, and

353   less extensive offshore along path B, ~ 100-200 km from the slope (Fig.2f).

354   We have presented here only the dissipation for the M2 harmonic, but in the rest of the

355   paper, we will analyze the temperature fields on a seasonal scale and by this fact, the effect of

356   all the tidal harmonics on the temperature are considered.

357   **III.2. SST Validation**

358   Figure 3 shows the mean SST from TMI SST, tidal simulation and non-tidal simulation

359   over the entire 2013-2015 period. The mean SST of the tidal simulation (Fig.3b) reproduces

360   well spatially the TMI SST observations (Fig.3a) both for cooling on the shelf around 47.5°W

361   and to the southeast between 40°W–35°W and 2°S–2°N, which is almost absent for the non-

362   tidal simulation (Fig.3c). To the northeast, between 50°W–54°W and 3°N–8°N in the Amazon

363   plume, the SST of the non-tidal simulation is in better agreement with the observations, while

364   the SST of the tidal simulation is about 1 °C cooler than TIM SST. Such a difference is very

365   similar to what is obtained by other models in the same region (Hernandez et al., 2016, 2017;

366   Gévaudan et al., 2022). The seasonal cycle of the SST of the three products for the three years

367   2013-2015 (Fig.3d) is obtained by interpolating the SST of both simulations on the TMI SST

368   grid and averaging in the dashed boxes around the IT generation areas (Fig.3a, b, and c) with

369   the shelf being masked over the 200 m isobath. The tidal and non-tidal simulations of the model

370   reproduce well both the seasonal cycle and the standard deviation of the observations, with a

371   low RMSE of approximately 10^{-2} °C between each simulation and TMI SST (Fig.3d), which

372   indicates the good quality of our model simulations. Nevertheless, over the seasonal cycle, it

373   appears that between January-April and July-December, the tidal simulation is closer to the

374   observations, while the non-tidal simulation seems slightly warmer than the observations; and

375   in May-June, both simulations are colder than TMI SST (Fig.3d).

376   **IV.   Results**

377   In this section, we will present the influence of IT on the SST, the associated processes,

378   and the impact on the net atmosphere-ocean heat flux from the model's tidal and non-tidal

379   simulations. The analyses were performed on a seasonal scale between April-May-June (AMJ)

380   and August-September-October (ASO) for the three years 2013-2015.

381   **IV.1. Tide-enhanced surface cooling**

382   Beginning in July, a tongue of cold water (< 27 °C) begins to form to the southeast and

383   enters the central part of the plateau in August and remains there until October. Figure 3e-g

384   show the SST, averaged over the ASO season. The tidal simulation (Fig.3f) shows that the

385   upwelling cell, represented by the extension of the 27.2 °C isotherm along the slope to about

386   49°W–3°N, extends further north than in the non-tidal simulation (Fig.3g, 45°W–0°N) which

387   is in better agreement with the TMI SST observations over the same period (Fig.3e).

388   The general impact of the tide, illustrated by showing the difference in SST between

389   the tidal and the non-tidal simulations in both seasons (Fig.4c-d, respectively for AMJ and

390   ASO), is a cooling over a large part of the study area with maxima (up to -0.3 °C): in the

391   Amazon plume downstream of the river mouth (northeast beyond 3°N), and on the path of

392   propagation of IT for both seasons. For ASO, tides induce a warming (> +0.3 °C) on the shelf

393   at the mouth of the Amazon River, while for AMJ it is a cooling (-0.3 °C). East of 45°W, the

394   tide-induced cooling for each of the two seasons has different spatial structures, but this is

395   probably due to different mesoscale variability between the two seasons.

396   **IV.2. Impact in the Atmosphere–Ocean Net heat flux (Q_T)**

397   Associated with the cooling of the SST, the tide induces Qt anomalies whose spatial

398   structure is very similar to the SST. Indeed, the difference in Qt is essentially positive over the

399   whole domain during the AMJ season (Fig.4a) with average maximum values around 25 W.m^{-2}

400   in the plume and the Amazon retroflection to the northeast and along A and B. During the ASO

401   season, there is as for the temperature at the mouth of the Amazon an inverse anomaly of -25

402   W.m^{-2} (Fig.4b). In each season, the spatial structure of the Qt difference almost perfectly

403   matches that of the SST difference. Knowing that the atmosphere and the underlying ocean are

404   in a certain equilibrium, the cooling of the SST by the water masses arriving at the surface will

405   disturb this balance. In response, a consequent variation of the net heat flux from the

406   atmosphere to the ocean, will try to restore the balance. As shown by the very strong and

407   significant negative correlation between the difference in Qt and the difference in SST. For the

408   AMJ season, we have a negative correlation of -0.97 with a significance of $R^2 = 0.95$, and about

409   the same as for the ASO season with -0.98 and 0.96 respectively for negative correlation and

410   its significance (Fig.9f).

411   The integral over the entire domain of the net heat flux for each season and for each

412   simulation (Fig.4e) shows that during the AMJ season, the Qt increases from 23.85 TW for the

413   non-tidal simulation to 35.7 TW for the tidal simulation, an increase of +33.2 %, two times

414   greater than that found (15 %) by Tchilibou et al. (2020) in Solomon Sea. Thus, the tide and IT

415   are responsible for a third of the variation in net atmosphere-ocean heat flux during this season.

416   While during the second ASO season, there is a smaller increase in Qt of +7.4%, i.e., a variation

417   from 73.03 TW to 78.83 TW between the non-tidal and tidal simulations.

418   We also note the considerable difference in integrated Qt between seasons. We start
419   from values below 36 TW in the AMJ season to values above 73 TW in the ASO season, i.e.,
420   a multiplication by a factor of at least order 2. These larger values could probably be related
421   with the appearance of the upwelling cell described above, knowing that cooler SSTs induce
422   stronger Qt.

IV.3. Vertical structure of the Temperature along A

424   To further analyze the temperature changes between both simulations, we made vertical
425   sections following the path of IT emanating from sites A and B (blue and red line in Figure 2e
426   respectively). We will show only the results following path A, but the results are similar for
427   path B.

428   Figure 5 shows vertical sections of temperature for the two seasons following A. For
429   the AMJ season, over the slope and near the coast, cold water (< 27.6 °C) remains below the
430   surface at ~ 20 m for the tidal simulation (Fig.5a) and deeper at ~ 60 m for the non-tidal
431   simulation (not shown), it then rises to the surface more than 400 km offshore for both
432   simulations. Although at the surface the difference in SST between the two simulations (tide -
433   no-tide) is relatively small (~ -0.3 °C, Fig.4c), because the SST is damped by the heat fluxes,
434   further down the water column, this difference becomes much larger (> ± 1.2 °C, Fig.5c).
435   Above the thermocline (< 120 m, cyan and yellow lines in Fig.5c), the simulation with the tides
436   is colder by 1.2 °C from the slope where the IT are generated to the open ocean following their
437   propagation path. Conversely, below the thermocline, the tidal simulation is warmer by +1.2
438   °C up to ~ 300 m along the same propagation path. During this AMJ season, the thermocline
439   (~ 100 m ± 15 m, thick dashed black line, Fig.5a) and the mixing layer (~ 40 m ± 20 m, thick
440   dashed white line, Fig.5a) have a very weak slope between the coast and the open ocean.
441   Furthermore, the difference in isodensity depths between the two simulations is small (not
442   shown), as are the depths of the thermocline (~ 10 m, Fig.5c) and the mixing layer (not shown),
443   although these different depths are closer to the surface for the tidal simulation (not shown).
444   Over the whole domain (not shown), the thermocline is deeper by 15 m on average in the non-
445   tidal simulation, following the propagation paths of the IT energy flow, on the Amazon shelf
446   and plume. While the mixing layer in the non-tidal simulation is deeper by an average of 13 m
447   over the shelf, 4 m on average along the IT propagation paths and close to zero in the Amazon
448   plume.

449   During the ASO season, cold waters (< 27.6 °C) previously confined below the surface
450   during the previous season (AMJ) then rise to the surface. These cold waters extend over the

451   slope and up to about 150 km offshore in the non-tidal simulation (not shown) and up to 250

452   km offshore in the tidal simulation (Fig.5b). The isotherm 27.2 °C reaches the surface above

453   the slope in the tidal simulation but remains below the surface (~ 30 m) in the non-tidal

454   simulation (not shown). At the surface and in the surface layers, the temperature in the presence

455   of the tide and IT is therefore cooler. The temperature difference between the two simulations

456   in the ASO season (Fig.5d) is smaller (< 0.4 °C) in the surface layers (< 40 m) near the coast

457   compared to the AMJ season (Fig.5c). In contrast, during the ASO season, this cooling reaches

458   the surface and results in a colder SST (-0.3 °C) (Fig.4d) along A. The strongest cooling (~ -

459   1.2 °C) is deeper between 60 and 140 m depth. Below the thermocline, warming (+1.2 °C) is

460   also present, but extends slightly less (~ 650 km) offshore (Fig.5d) compared to the AMJ season

461   (~ 1000 km, Fig.5c). During this ASO season, the coastward slope of the thermocline and

462   mixing layer becomes somewhat steeper compared to the other season. In both simulations,

463   there is a dip of ~ 80 m (~60 m offshore and ~140 m inshore) and ~40 m (~30 m offshore and

464   ~70 m inshore), respectively for the thermocline (thick dashed black line, Fig.5b) and the

465   mixing layer (thick dashed white line, Fig.5b). Over the entire domain (not shown) between

466   the two simulations (tide - no-tide), the tide deepens the thermocline depth by +6 m on the shelf

467   and +12 m at the plume and along the propagation path of A. As for the mixing layer, which is

468   deeper in the tidal run by 12 m along the shelf and along the propagation path of A.

469   Between the two seasons, there is also a change in the vertical density gradient between

470   the coast and the open sea. In the simulation with tide (Fig.5a) and without tide (not shown),

471   during the AMJ season, a strong vertical density gradient is present near the coast and decreases

472   towards the open sea. In contrast, during the second ASO season, the vertical density gradient

473   is weaker inshore than offshore. This clearly highlights a seasonality in the vertical density

474   gradient profile in agreement with Tchilibou et al. (2022). The transect of the temperature

475   differences between the two simulations (Fig.5c-d) show that IT (and probably the tide) can

476   influence the temperature in the ocean from the surface to the bottom, with a greater effect on

477   the first 300 meters. One question we address in this paper is to better understand what

478   processes are at work that explain these temperature changes.

479   **IV.4. Processes involved modifying the temperature**

480   To explain the observed surface and water column temperature changes, we calculated

481   the trend terms of the temperature evolution equation (see Section II.3.2, Equation 6) for both

482   seasons (AMJ and ASO) also averaged over the three years from 2013 to 2015.

IV.4.1. Vertical diffusion of Temperature

Figure 6 shows the vertical temperature diffusion term (ZDF) for both seasons AMJ (left panel) and ASO (right panel). The ZDF is averaged between 2–20 m, i.e., within the mixing layer depth range. For the AMJ season, the ZDF of the tidal simulation (Fig.6a) shows a negative trend (cooling) in the whole domain, which is maximum on the continental slope where the IT are generated and on their propagation path (< - 0.4 °C.day^{-1}), with larger horizontal extent along A (~700 km from the coasts) compared to B (~300 km from the coasts). Over the rest of the domain, it remains very low (> - 0.1 °C.day^{-1}). For the non-tidal simulation (Fig.6c), the ZDF is very weak (> - 0.1 °C.day^{-1}) over the entire domain, demonstrating that internal tidal waves would be the main driver of the vertical temperature diffusion in this region during this season. For the second ASO season, the tidal simulation (Fig.6b) shows a decrease of the ZDF along the coast and a strengthening offshore following A, but with the same cooling trend (< -0.4 °C.day^{-1}). While along B, it becomes almost closed to zero, both at the coast and offshore (Fig.6b). In addition, the mesoscale circulation intensifies during this season. Therefore, to the northeast, approximately between 4°N–8°N, and 47°W–53°W, there is a cooling on the shelf (~ +0.3 °C.day^{-1}) with NBCR-like patterns, both in the tidal simulation (Fig.6b) and in the non-tidal simulation (Fig.6d).

On the vertical following A, we notice an inter-thermocline vertical profile for the simulation with tide in the two seasons AMJ and ASO (respectively Fig.6e and 6f), with a cooling tendency (< -0.4 °C.day^{-1}) above the thermocline and a warming (> +0.4 °C.day^{-1}) below the thermocline, with an average vertical extension of ~ 350 m depth for the maximum values, but which exceeds 500 m depth for the low values (< +0.1 °C.day^{-1}). Over the slope, we see, as for the horizontal averages, this weakening of the ZDF between the AMJ (Fig.6e) and ASO (Fig.6f) seasons and the strengthening offshore. On the other hand, on the vertical, we observe towards the open sea (> 200 km) that the ZDF maxima seem to be discontinuous and spaced of about 120–150 km during the AMJ season (Fig.6e), while we have a more continuous diffusion for the ASO season (Fig.6f). This is consistent with the ZDF vertical averages (Fig.6a-b). For the non-tidal simulation, the vertical temperature diffusion tends towards 0 °C.day^{-1} within the water column but remains quite large (> -0.2 °C.day^{-1}) in the thin surface layer (Fig.6g-h).

During the AMJ season, the ITCZ is close to the equator and thus the trade Winds have their maximum intensity in the heart of the domain, while they migrate northward for the ASO season. As a result, more wind-generated diapycnal mixing is expected in the domain during

516 the AMJ season compared to the ASO season. But the average value of the ZDF ($\sim$ -0.2

517 °C.day^{-1}) is the same between the two seasons and for both simulations (not shown) over most

518 of the domain (except for the areas of the NBC backscatter for both simulations, on IT's

519 generation sites and on their propagation path for the tidal simulation). This implies that the

520 ability of the wind to generate diapycnal mixing in the underlying ocean surface layer could be

521 limited by various oceanic processes in this region or is not well considered in the model.

522   Furthermore, it is important to note that along the IT propagation's pathway, the

523 maximum of the ZDF follows the maxima of the baroclinic tidal energy dissipation (Fig.2f).

524 Thus, the dissipation of IT generated on the continental slope generates vertical mixing that

525 enhances the cooling observed at the surface along the coast. In addition, this temperature

526 diffusion contributes to greater subsurface cooling, and warming in the deeper layers beneath

527 the thermocline.

528   In section IV.3 the seasonality of the vertical gradient of stratification was highlighted,

529 which is stronger at the coast relative to the open ocean during the AMJ season, and reverses

530 during the ASO season to become stronger offshore relative to the coast. This could explain

531 why the ZDF is stronger along the slope and along the near-coastal pathway B during the AMJ

532 season (Fig.6a), while it is weaker along the slope and closed to zero following B during the

533 ASO season (Fig.6b). The vertical gradient of density (and thus stratification) over the slope

534 influences the generation of IT, by controlling the propagation mode of the IT that are generated

535 (e.g.: Tchilibou et al., 2020 and Barbot et al., 2021). We show here that this vertical gradient

536 also plays on the fate of these IT, in this case on their dissipation. The vertical gradient of the

537 stratification thus determines where the internal tidal waves dissipate their energy in the water

538 column.

IV.4.2. Vertical advection of Temperature

540   The vertical temperature advection (z–ADV) averaged between 2–20 m is almost zero

541 in these surface layers throughout the region (Fig.7a, b, c, and d). For both seasons, some weak

542 extreme values are in the northwest on the plateau between 54°W–50°W and 3°N–3°N) and

543 are of the same intensity between the two simulations. With a slight intensification when

544 moving to the ASO season ($\sim$ -0.3 °C.day^{-1}). The z–ADV is zero at the IT generation sites and

545 along their propagation pathways, so the almost zero difference between the two simulations

546 for each season shows that the IT and barotropic tide do not generate vertical temperature

547 advection within these ocean surface layers. The z–ADV does not contribute to the temperature

548 change in the surface layers of the ocean, and therefore does not influence the cooling observed

549   from the surface on the SST. On the other hand, deeper, under the mixed layer and close to the

550   thermocline, the z–ADV structure is more marked.

551   Vertical sections following A (Fig.7e, f, g and h) show an intensification of z–ADV

552   below the mixing layer and near the thermocline between 80 and 200 m (~ ± 0.8 °C.day⁻¹).

553   During the AMJ season, over the vertical, the z–ADV appears to be rather dominated by a

554   cooling trend. The tidal simulation (Fig.7e) shows a cooling trend (~ -0.8 °C.day⁻¹), on the

555   slope where the IT are generated, with an average vertical extension from ~ 20 to 200 m depth.

556   Then offshore, two cooling hotspots (~ -0.8 °C.day⁻¹) followed by a weaker one (~ -0.3

557   °C.day⁻¹) spaced about 120–150 km apart, *separated* interspersed by two warming zones, respectively ~

558   +0.6 °C.day⁻¹ and ~ +0.3 °C.day⁻¹ from the coast. For the non-tidal simulation (Fig.7g), the z–

559   ADV is much less intense with lower values (< ± 0.3 °C.day⁻¹) near the coast until ~ 300 km

560   offshore, followed by a cooling hotspot (~ -0.8 °C.day⁻¹) between 300 km and 500 km. For

561   both simulations, the extreme values appear to be centered around the mean depth of the

562   thermocline (thick black outline) and do not cross the mixing layer depth (thick magenta

563   outline). They are on average located between 40 m and 200 m depth and follow the position

564   of the maximum vertical density gradient between isodensity anomalies 23.8–26.3 kg.m⁻³.

565   For the ASO season, the simulation with tide (Fig.7f) still shows the same cooling

566   intensity on the slope, although deeper (~ 60 m and 250 m), as well as offshore with this time

567   the third cooling hotspot more intense (~ -0.8 °C.day⁻¹) than during the AMJ season (Fig.7e).

568   The non-tidal simulation (Fig.7h) shows a less intense z–ADV (< ±0.1 °C.day⁻¹) near the slope,

569   and a little stronger offshore (~ ±0.3 °C.day⁻¹) between 300 and 600 km from the slope,

570   although less intense than the previous season.

571   As in the AMJ season, the extreme values of z–ADV follow the vertical density gradient

572   in both simulations. During the ASO season, the maximum of the vertical density gradient is

573   between 23.8 and 26.2 kg.m⁻³ ~~and~~ , is deeper at the coast and is closer to the surface offshore.

574   Thus, the extreme values of z–ADV are located a little deeper, between 80 and 300 m.

575   Furthermore, for the non-tidal simulation and during both seasons, the position relative to the

576   coast of the extreme values are shifted regarding those ones of the same polarity in the

577   corresponding tidal simulation, which means that the presence of the IT and the tides could

578   modify the intensity and patterns of the z–ADV produced by the other oceanic processes.

579   In addition, we averaged the z–ADV between deeper depths above the thermocline

580   depth (20–70 m) and below the thermocline (148–250 m) depth for all simulations and both

581   seasons (not shown). This allows to highlight the NBC's pathway through the extreme values

582   of the z–ADV close to the coast and its retroflection offshore to the northeast for both

583   simulations, but also the propagation of the IT from the coast to the open sea from the two main

584   sites A and B for the simulation with tide. Thus, we see that the IT and the general circulation

585   are the main drivers of the vertical temperature advection in the subsurface and deeper layers

586   in this region.

IV.4.3. Horizontal advection of temperature

588   Horizontal advection of temperature (h–ADV) is defined as the sum of the zonal (x–

589   ADV) and meridional (y–ADV) terms of temperature advection. The h–ADV is also averaged

590   between 2–70 m for each simulation during both seasons (Fig.8a, b, c and d). As obtained with

591   z–ADV, horizontal advection of temperature tends to zero over the entire domain in the surface

592   layers for both seasons in both simulations, with some weak extreme values located in the

593   northwest on the plateau between 54°W–50°W and 3°N–3°N) that intensify during the ASO

594   season (~ ±0.2 °C.day⁻¹) (Fig.8b and d). Along the slope between sites A and B during the AMJ

595   season, the h–ADV generates a small warming (~ +1 °C.day⁻¹) that is more pronounced in the

596   tidal simulation (Fig.8a) than in the non-tidal simulation (Fig.8c), and thus appears to be related

597   to the IT generated along the slope. On the other hand, the small difference between the two

598   simulations in the surface layers shows that the tidal processes (IT and barotropic tide) hardly

599   generate horizontal temperature advection. The low values observed here clearly show that the

600   h–ADV could not influence the cold-water tongue observed over the surface SST (Fig.3e-g)

601   during the ASO season.

602   Along the vertical following A, the h-ADV maxima remain essentially confined below

603   the mixing layer, with much more intense values in the tidal simulation compared to the non-

604   tidal simulation. The h–ADV contributes to both warming and cooling of the temperature (~

605   ±0.4 °C.day⁻¹) from the slope to more than 500 km offshore, with an average vertical extension

606   between the surface and 400 m depth for the tidal simulation (Fig.8e and f) and a little less

607   extended between 20–300 m depth for the non-tidal simulation (Fig.8g and h) during both

608   seasons. The h–ADV ~~which~~ is low in the surface layers (2–20 m) but maximum in the

609   subsurface where the stratification is stronger. We also see for the tidal simulation in both

610   seasons a warming above the slope that reaches the surface with an intensity of about +0.4

611   °C.day⁻¹ (Fig.8e and f) but remains below the surface (~ 20 m) in the non-tidal simulation

612   (Fig.8g and h). This vertical excursion that is observed elsewhere for ZDF and z–ADV is a

613   marker of local dissipation of IT at their generation site on the slope, which clearly affects both

614   vertical diffusion and advection of the temperature. But we have almost null values along the

615   slope when averaging h–ADV or z–ADV between 2-20 m and much more strong values for
616   the ZDF (Fig.6a, b, c and d). This means that the IT's energy loss is mostly transferred to the
617   turbulent scale (mixing). Furthermore, unlike the ZDF (Fig.6e) and z–ADV (Fig.7e and f), on
618   the vertical it is difficult to identify a wave structure characteristic of IT propagation in the h-
619   ADV.

620   **V.   Summary and Discussions**

621   In this paper, the impact of internal tidal waves (IT) on temperature, off the Amazon,
622   especially on the surface and on net heat fluxes is explored through outputs of two twin oceanic
623   simulations (with and without tides) from a realistic model. The AMAZON36 configuration,
624   based on the 1/36° resolution NEMO model, can reproduce the generation of internal tides (IT),
625   i.e., the conversion of energy from barotropic to baroclinic tides, from two most energetic sites
626   A and B, in good agreement previous studies (Magalhaes et al., 2016 and Tchilibou et al.,
627   2022). As for dissipation, the model reproduces 30% local dissipation, the rest propagating
628   offshore from the different generation sites, the two main ones being A and B (Fig.2e). During
629   their propagation, the IT dissipate most of their energy after two beams of mode-1 reflection
630   (120–150 km), that is less than 300 km from the slope.

631   The analyses are based on data from three years (2013 to 2015), averaged over two
632   seasons, AMJ (April-May-June) and ASO (August-September-October) which are highly
633   contrasted in terms of stratification, circulation and EKE. During ASO, the cold waters (< 27.5
634   °C) of the Atlantic Cold Tongue (ACT) enter our domain along the coast, and are affected by
635   IT and tides, which leads to a cooler seasonal upwelling.

636   The impact of the tides on temperature was assessed by comparing our twin simulations
637   with and without tides for each season. For ASO and AMJ, the tides create a cooling of SST of
638   the order of $\sim$ -0.3 °C in the plume of the Amazon offshore and along the paths of propagation
639   A and B of the internal tide. Concerning the Amazon shelf, the tides induce a warming ($\sim$ +0.3
640   °C) in ASO and a cooling (of $\sim$ -0.3 °C) in AMJ. These cooler/warmer waters are responsible
641   in the same location for an increase/decrease in the net heat flux from the atmosphere to the
642   ocean, leading to an increase (Qt) of +33.2% in AMJ and of +7.4% in ASO between runs with
643   and without tides. In the subsurface, above the thermocline (<120 m), the IT and tides induce
644   a stronger cooling than on the surface of about $\sim$ -1.2 °C and an associated warming of about
645    $\sim$ +1.2 °C under the thermocline (>120 m to 300 m).

646   By increasing the atmosphere to ocean net heat flux (Qt), the IT and tides might reduce
647   the cloud convection in the atmosphere, as we are in an intertropical convergence zone (ITCZ).

648   Impact on overall atmospheric circulation and precipitation is expected to be significant, as
649   previously shown in other regions such as Indonesia (Tidal induced cooling of -0.3 °C can
650   reduce precipitation by -20%, see Koch-Larrouy et al., 2010).

651   Therefore, it becomes important to note that the interannual or even climatic scale
652   evolution of internal tidal waves activity must be considered to better understand the future
653   evolution of the global climate. Especially since thanks to the CanESM5 global climate model,
654   Yadidya and Rao (2022) have just shown that in the Andaman Sea and Bay of Bengal, towards
655   the end of this century, for both optimistic and pessimistic SSP scenarios, the increase in depth-
656   averaged stratification will result in an increase in IT activity in these two regions. Knowing
657   that the continental slope of northern Brazil is a place of high generation of IT, which therefore
658   depends on stratification, it is hereby critical to understand how IT activity will evolve in the
659   coming decades in order to better anticipate the climate, and thus better adapt public policies
660   at national and international levels to the global context of climate change.

661   Another objective of our study was to understand the processes responsible for these
662   temperature changes. For this, we analyzed the trend terms of the temperature evolution
663   equation. Where IT dissipate their energy, there is an intense vertical mixing that generates
664   vertical diffusion of temperature (ZDF) (-0.4 °C.day^{-1}) according to pathway A and to a lesser
665   extent according to pathway B, stronger at shore than offshore during AMJ and inverse during
666   ASO. The ZDF is the only process that reaches the surface layer, and then appears in first
667   approximation to be the main process contributing to the surface cooling observed on SST. The
668   atmospheric heat flux terms (FOR_Z) could also modify this SST but was not highlighted in this
669   study. The mixing takes place up to about 800 km off the slope following A, and 300 km
670   following B. It is also responsible on a seasonal scale, but also daily for a negative average
671   variation (cooling) of temperature of about -0.4 °C.day^{-1} above the thermocline, and a warming
672   of +0.4 °C.day^{-1} below 350 m and decreasing to +0.1 °C.day^{-1} around 500 m depth.

673   IT propagation induce vertical advection of water masses around the thermocline level,
674   which has the effect of producing a subsurface mean temperature cooling (~ -0.8 °C.day^{-1}) at
675   a depth varying between 20–200 m AMJ and 60–250 m in ASO, with three extreme values off
676   the coast spaced approximately 120–150 km along of the pathway A, which seem to follow the
677   dissipation patterns, and thus correspond to the horizontal scale of the mode-1 propagation of
678   IT. Other processes such as zonal and meridional advection of temperature also induce
679   temperature change in subsurface and deeper layers. Finally, the horizontal (zonal and

680   meridional) advection of temperature in this region is more related to the general circulation

681   (NBC, mesoscale) but is increased by tides and IT.

682   Thus, it is the combination of these different processes that explains the temperature

683   change in the water column in this region. Furthermore, in order to explain the cooling of the

684   SST at the surface, Neto et al. (2014) indicated that the northward transport of water masses by

685   the constant circulation of the NBC was compensated by a vertical advection of colder water

686   masses towards the surface. We now know that this vertical advection process fails to modify

687   the SST but is rather limited below the mixing layer. The same is true for zonal and meridional

688   advection of temperature (which form horizontal advection). It should be remembered that

689   vertical diffusion extends from the surface, through the mixing layer, into the deep layers. It is

690   therefore possible that water masses cooled by both vertical and horizontal advection below

691   the mixing layer can be recovered and transported vertically to the surface by the effect of

692   vertical mixing. The change in SST and temperature above the mixing layer then comes from

693   (i) vertical diffusion of temperature and (ii) a combination of this vertical diffusion and the

694   advection (vertical and horizontal) of temperature that takes place below the mixing layer.

695   This study focuses on temperature, but other analyses we have done on salinity show

696   that IT also affects the haline structure of the ocean in this region. A future work would be to

697   look at the impact on salinity, which is also a key parameter in the functioning of the ocean as

698   in exchanges with the atmosphere, and thus can play a role on the climate. In addition, internal

699   waves can also influence the biogeochemical cycles of elements and the entire marine

700   ecosystem, since they can induce nutrient uptake and thus participate in structuring the spatial

701   distribution of phytoplankton and zooplankton, and in consequence of the rest of the food chain

702   that depends on them.

703   It would also be important to compare the results of our model with fields observations.

704   Two high frequency PIRATA anchorages have been installed offshore at the extremity of our

705   region between 35°W–38°W and 0°N–5°N (see Bourlès et al. 2019) and could be used for this

706   purpose. In addition, recently, the "*AMAZOMIX*" campaign entirely dedicated to IT (27 August

707   and 8 October 2021) will provide a better understanding of the impact of IT on the marine

708   environment in this region. In the meantime, a coupled physical/biogeochemistry simulation

709   (NEMO/PISCES), currently under analysis, will begin to answer these crucial questions of the

710   impact of internal waves on biogeochemistry.

711   Finally, in this first part, we have focused on describing the effects of internal tidal
712 waves on temperature variation on a seasonal scale, while the remainder of this work will
713 address temperature changes on finer time scales, notably on the tidal scale.
714
715

Data availability

717   The TMI SST v7.1 data are publicly available online from the REMSS platform:
718 https://www.remss.com/missions/tmi/, was accessed on 27 June 2022. The model simulations
719 are available upon request by contacting corresponding authors.

Authors contributions

721   Funding acquisition, AKL; Conceptualization and methodology, FA, AKL and ID.
722 Numerical simulations, GM and FA. Formal analysis, FA; FA prepared the paper with
723 contribution from all co-authors.

Competing interests

725   The authors declare that they have no conflict of interest.
726

Acknowledgments

728   This work is part of the Fernand Assene PhD thesis, cofounded by Institut de Recherche
729 pour le Développement (IRD) and Mercator Ocean International (MOi). The numerical
730 simulation was founded by CNRS/CNES/IRD via the projects A0080111357 and
731 A0130111357 and were performed tank to the IDRIS platform calculator (Jean-Zay).

Abbreviations

733 The following abbreviations are used in this manuscript:
734 AMASSEDS: A Multi-disciplinary Amazon Shelf SEDiment Study
735 AMAZOMIX: AMAZOn MIXing
736 FES2012 | FES2014: Finite Element Solution 2012 | Finite Element Solution 2014
737 NEMO/PISCES: Nucleus for European MOdeling / Pelagic Interactions Scheme for Carbon
738 and Ecosystem Studies
739 PIRATA: PredIction and Research moored Array in the Tropical Atlantic
740 REVIZEE : Recursos Vivos da Zona Econômica Exclusiva
741

References

Aguedjou, H.M.A., Chaigneau, A., Dadou, I., Morel, Y., Pegliasco, C., Da-Allada, C.Y., Baloïtcha, E., 2021. What Can We Learn From Observed Temperature and Salinity Isopycnal Anomalies at Eddy Generation Sites? Application in the Tropical Atlantic Ocean. Journal of Geophysical Research: Oceans 126, e2021JC017630. https://doi.org/10.1029/2021JC017630

Aguedjou, H.M.A., Dadou, I., Chaigneau, A., Morel, Y., Alory, G., 2019. Eddies in the Tropical Atlantic Ocean and Their Seasonal Variability. Geophysical Research Letters 46, 12156–12164. https://doi.org/10.1029/2019GL083925

Araujo, M., Dimoune, D.M., Noriega, C., Hounsou-Gbo, G.A., Veleda, D., Araujo, J., Bruto, L., Feitosa, F., Flores-Montes, M., Lefèvre, N., Melo, P., Otsuka, A., Travassos, R.K., Schwamborn, R., Neumann-Leitão, S., 2021. Camadas Finas III - BR cruise: S-ADCP data. https://doi.org/10.17882/80828

Araujo, M., Noriega, C., Hounsou-gbo, G.A., Veleda, D., Araujo, J., Bruto, L., Feitosa, F., Flores-Montes, M., Lefèvre, N., Melo, P., Otsuka, A., Travassos, K., Schwamborn, R., Neumann-Leitão, S., 2017. A Synoptic Assessment of the Amazon River-Ocean Continuum during Boreal Autumn: From Physics to Plankton Communities and Carbon Flux. Frontiers in Microbiology 8.

Araujo, J.; Mezilet, Y.; Marin, F.; Jouanno, J.; Araujo, M. On the variability of the upwelling cell off the Amazon River mouth (01072-00001). In: VII Congresso Brasileiro de Oceanografia - CBO2016, 2016, Salvador, BA. Livro de Resumos - CBO2016. Salvador, BA: AOCEANO, 2016. v. 1.

Arbic, B., Richman, J., Shriver, J., Timko, P., Metzger, E., Wallcraft, A., 2012. Global Modeling of Internal Tides Within an Eddying Ocean General Circulation Model. Oceanography 25, 20–29. https://doi.org/10.5670/oceanog.2012.38

Archer, D., Martin, P., Buffett, B., Brovkin, V., Rahmstorf, S., Ganopolski, A., 2004. The importance of ocean temperature to global biogeochemistry. Earth and Planetary Science Letters 222, 333–348. https://doi.org/10.1016/j.epsl.2004.03.011

Barbot, S., Lagarde, M., Lyard, F., Marsaleix, P., Lherminier, P., Jeandel, C., 2022. Internal Tides Responsible for Lithogenic Inputs Along the Iberian Continental Slope. Journal of Geophysical Research: Oceans 127, e2022JC018816. https://doi.org/10.1029/2022JC018816

774 Barbot, S., Lyard, F., Tchilibou, M., Carrere, L., 2021. Background stratification impacts
775   on internal tide generation and abyssal propagation in the western equatorial Atlantic
776   and the Bay of Biscay. Ocean Science 17, 1563–1583. https://doi.org/10.5194/os-17-
777   1563-2021

778 Barton, E.D., Inall, M.E., Sherwin, T.J., Torres, R., 2001. Vertical structure, turbulent
779   mixing and fluxes during Lagrangian observations of an upwelling filament system
780   off Northwest Iberia. Progress in Oceanography, Lagrangian studies of the Iberian
781   upwelling system 51, 249–267. https://doi.org/10.1016/S0079-6611(01)00069-6

782 Beardsley, R.C., Candela, J., Limeburner, R., Geyer, W.R., Lentz, S.J., Castro, B.M.,
783   Cacchione, D., Carneiro, N., 1995. The M2 tide on the Amazon Shelf. Journal of
784   Geophysical Research: Oceans 100, 2283–2319. https://doi.org/10.1029/94JC01688

785 Bordois, L., Auclair, F., Paci, A., Dossmann, Y., Gerkema, T., Nguyen, C., 2016. Tidal
786   energy redistribution among vertical modes in a fluid with a mid-depth pycnocline.
787   Physics of Fluids 28, 101701. https://doi.org/10.1063/1.4964759

788 Bourles, B., Molinari, R.L., Johns, E., Wilson, W.D., Leaman, K.D., 1999. Upper layer
789   currents in the western tropical North Atlantic (1989–1991). Journal of Geophysical
790   Research: Oceans 104, 1361–1375. https://doi.org/10.1029/1998JC900025

791 Buijsman, M.C., Ansong, J.K., Arbic, B.K., Richman, J.G., Shriver, J.F., Timko, P.G.,
792   Wallcraft, A.J., Whalen, C.B., Zhao, Z., 2016. Impact of Parameterized Internal Wave
793   Drag on the Semidiurnal Energy Balance in a Global Ocean Circulation Model.
794   Journal of Physical Oceanography 46, 1399–1419. https://doi.org/10.1175/JPO-D-
795   15-0074.1

796 Buijsman, M.C., Arbic, B.K., Richman, J.G., Shriver, J.F., Wallcraft, A.J., Zamudio, L.,
797   2017. Semidiurnal internal tide incoherence in the equatorial Pacific. Journal of
798   Geophysical   Research: Oceans   122,   5286–5305.
799   https://doi.org/10.1002/2016JC012590

800 Carrere, L., Lyard, F., Cancet, M., Guillot, A., & Roblou, L. (2012). FES 2012: A new
801   global tidal model taking advantage of nearly 20 years of altimetry, in 20 Years of
802   Progress in Radar Altimetry.

803 Clayson, C.A., Bogdanoff, A.S., 2013. The Effect of Diurnal Sea Surface Temperature
804   Warming on Climatological Air–Sea Fluxes. American Meteorological Society.

805 Collins, M., An, S.-I., Cai, W., Ganachaud, A., Guilyardi, E., Jin, F.-F., Jochum, M.,
806   Lengaigne, M., Power, S., Timmermann, A., Vecchi, G., Wittenberg, A., 2010. The

807   impact of global warming on the tropical Pacific Ocean and El Niño. Nature Geosci

808   3, 391–397. https://doi.org/10.1038/ngeo868

809   da Silva, J.C.B., New, A.L., Srokosz, M.A., Smyth, T.J., 2002. On the observability of

810   internal tidal waves in remotely-sensed ocean colour data. Geophysical Research

811   Letters 29, 10-1-10–4. https://doi.org/10.1029/2001GL013888

812   de Macedo, C.R., Koch-Larrouy, A., da Silva, J.C.B., Magalhães, J.M., Lentini, C.A.D.,

813   Tran, T.K., Rosa, M.C.B., Vantrepotte, V., 2023. Spatial and temporal variability of

814   mode-1 and mode-2 internal solitary waves from MODIS/TERRA sunglint off the

815   Amazon shelf. EGUsphere 1–27. https://doi.org/10.5194/egusphere-2022-1482

816   Demaster, D.J., Pope, R.H., 1996. Nutrient dynamics in Amazon shelf waters: results from

817   AMASSEDS. Continental Shelf Research 16, 263–289. https://doi.org/10.1016/0278-

818   4343(95)00008-O

819   Denman, K.L., Gargett, A.E., 1983. Time and space scales of vertical mixing and

820   advection of phytoplankton in the upper ocean. Limnology and Oceanography 28,

821   801–815. https://doi.org/10.4319/lo.1983.28.5.0801

822   Didden, N., Schott, F., 1993. Eddies in the North Brazil Current retroflection region

823   observed by Geosat altimetry. Journal of Geophysical Research: Oceans 98, 20121–

824   20131. https://doi.org/10.1029/93JC01184

825   Dimoune, D. M., Birol, F., Hernandez, F., Léger, F., Araujo, M., 2022. Revisiting the

826   tropical Atlantic western boundary circulation from a 25-year time series of satellite

827   altimetry data. *EGUsphere*, 1-42.

828   Egbert, G.D., Ray, R.D., 2000. Significant dissipation of tidal energy in the deep ocean

829   inferred   from   satellite   altimeter   data.   Nature   405,   775–778.

830   https://doi.org/10.1038/35015531

831   Gabioux, M., Vinzon, S.B., Paiva, A.M., 2005. Tidal propagation over fluid mud layers

832   on   the   Amazon   shelf.   Continental   Shelf   Research   25,   113–125.

833   https://doi.org/10.1016/j.csr.2004.09.001

834   Garzoli, S.L., Ffield, A., Johns, W.E., Yao, Q., 2004. North Brazil Current retroflection

835   and   transports.   Journal   of   Geophysical   Research: Oceans   109.

836   https://doi.org/10.1029/2003JC001775

837   Garzoli, S.L., Ffield, A., Yao, Q., 2003. North Brazil Current rings and the variability in

838   the latitude of retroflection, in: Goni, G.J., Malanotte-Rizzoli, P. (Eds.), Elsevier

839   Oceanography Series, Interhemispheric Water Exchange in the Atlantic Ocean.
840   Elsevier, pp. 357–373. https://doi.org/10.1016/S0422-9894(03)80154-X

841   Gévaudan, M., Durand, F., Jouanno, J., 2022. Influence of the Amazon-Orinoco Discharge
842   Interannual Variability on the Western Tropical Atlantic Salinity and Temperature.
843   Journal   of   Geophysical   Research: Oceans   127,   e2022JC018495.
844   https://doi.org/10.1029/2022JC018495

845   Geyer et al., 1996. Physical oceanography of the Amazon shelf. Continental Shelf
846   Research 16, 575–616. https://doi.org/10.1016/0278-4343(95)00051-8

847   González-Haro, C., Ponte, A., Autret, E., 2019. Quantifying Tidal Fluctuations in Remote
848   Sensing   Infrared   SST   Observations.   Remote   Sensing   11,   2313.
849   https://doi.org/10.3390/rs11192313

850   Heathershaw, A.D., New, A.L., Edwards, P.D., 1987. Internal tides and sediment transport
851   at the shelf break in the Celtic Sea. Continental Shelf Research 7, 485–517.
852   https://doi.org/10.1016/0278-4343(87)90092-6

853   Hernandez, O., Jouanno, J., Durand, F., 2016. Do the Amazon and Orinoco freshwater
854   plumes really matter for hurricane-induced ocean surface cooling? Journal of
855   Geophysical   Research: Oceans   121,   2119–2141.
856   https://doi.org/10.1002/2015JC011021

857   Hernandez, O., Jouanno, J., Echevin, V., Aumont, O., 2017. Modification of sea surface
858   temperature by chlorophyll concentration in the Atlantic upwelling systems. Journal
859   of   Geophysical   Research: Oceans   122,   5367–5389.
860   https://doi.org/10.1002/2016JC012330

861   Hersbach, H., Bell, B., Berrisford, P., Hirahara, S., Horányi, A., Muñoz-Sabater, J.,
862   Nicolas, J., Peubey, C., Radu, R., Schepers, D., Simmons, A., Soci, C., Abdalla, S.,
863   Abellan, X., Balsamo, G., Bechtold, P., Biavati, G., Bidlot, J., Bonavita, M., De
864   Chiara, G., Dahlgren, P., Dee, D., Diamantakis, M., Dragani, R., Flemming, J.,
865   Forbes, R., Fuentes, M., Geer, A., Haimberger, L., Healy, S., Hogan, R.J., Hólm, E.,
866   Janisková, M., Keeley, S., Laloyaux, P., Lopez, P., Lupu, C., Radnoti, G., de Rosnay,
867   P., Rozum, I., Vamborg, F., Villaume, S., Thépaut, J.-N., 2020. The ERA5 global
868   reanalysis. Quarterly Journal of the Royal Meteorological Society 146, 1999–2049.
869   https://doi.org/10.1002/qj.3803

870   HYBAM (2018) Contrôles géodynamique, hydrologique et biogéochimique de
871   l'érosion/altération et des transferts de matière dans les bassins de l'Amazone, de
872   l'Orénoque et du Congo. http://www.ore-hybam.org. Accessed 10 December 2021

873   Jackson, C., 2007. Internal wave detection using the Moderate Resolution Imaging
874   Spectroradiometer (MODIS). Journal of Geophysical Research: Oceans 112.
875   https://doi.org/10.1029/2007JC004220

876   Jayakrishnan, P.R., Babu, C.A., 2013. Study of the Oceanic Heat Budget Components over
877   the Arabian Sea during the Formation and Evolution of Super Cyclone, Gonu 2013.
878   https://doi.org/10.4236/acs.2013.33030

879   Jithin, A.K., Francis, P.A., 2020. Role of internal tide mixing in keeping the deep
880   Andaman Sea warmer than the Bay of Bengal. Sci Rep 10, 11982.
881   https://doi.org/10.1038/s41598-020-68708-6

882   Johns, W.E., Lee, T.N., Beardsley, R.C., Candela, J., Limeburner, R., Castro, B., 1998.
883   Annual Cycle and Variability of the North Brazil Current. Journal of Physical
884   Oceanography   28,   103–128.   https://doi.org/10.1175/1520-
885   0485(1998)028<0103:ACAVOT>2.0.CO;2

886   Johns, W.E., Lee, T.N., Schott, F.A., Zantopp, R.J., Evans, R.H., 1990. The North Brazil
887   Current retroflection: Seasonal structure and eddy variability. Journal of Geophysical
888   Research: Oceans 95, 22103–22120. https://doi.org/10.1029/JC095iC12p22103

889   Jouanno, J., Marin, F., Du Penhoat, Y., Sheinbaum, J., & Molines, J. M., 2011. Seasonal
890   heat balance in the upper 100 m of the equatorial Atlantic Ocean. Journal of
891   Geophysical Research: Oceans, 116(C9).

892   Kelly, S.M., Nash, J.D., Kunze, E., 2010. Internal-tide energy over topography. Journal of
893   Geophysical Research: Oceans 115. https://doi.org/10.1029/2009JC005618

894   Koch-Larrouy, A., Lengaigne, M., Terray, P., Madec, G., Masson, S., 2010. Tidal mixing
895   in the Indonesian Seas and its effect on the tropical climate system. Clim Dyn 34,
896   891–904. https://doi.org/10.1007/s00382-009-0642-4

897   Koch-Larrouy, A., Madec, G., Iudicone, D., Atmadipoera, A., Molcard, R., 2008. Physical
898   processes contributing to the water mass transformation of the Indonesian
899   Throughflow. Ocean Dynamics 58, 275–288. https://doi.org/10.1007/s10236-008-
900   0154-5

901   Koch-Larrouy, A., Madec, G., Bouruet-Aubertot, P., Gerkema, T., Bessières, L., Molcard,
902   R., 2007. On the transformation of Pacific Water into Indonesian Throughflow Water

903   by internal tidal mixing. Geophysical Research Letters 34.
904   https://doi.org/10.1029/2006GL028405
905   Kunze, E., MacKay, C., McPhee-Shaw, E.E., Morrice, K., Girton, J.B., Terker, S.R., 2012.
906   Turbulent Mixing and Exchange with Interior Waters on Sloping Boundaries. Journal
907   of Physical Oceanography 42, 910–927. https://doi.org/10.1175/JPO-D-11-075.1
908   Lambeck, K., Runcorn, S.K., 1977. Tidal dissipation in the oceans: astronomical,
909   geophysical and oceanographic consequences. Philosophical Transactions of the
910   Royal Society of London. Series A, Mathematical and Physical Sciences 287, 545–
911   594. https://doi.org/10.1098/rsta.1977.0159
912   Lascaratos, A., 1993. Estimation of deep and intermediate water mass formation rates in
913   the Mediterranean Sea. Deep Sea Research Part II: Topical Studies in Oceanography
914   40, 1327–1332. https://doi.org/10.1016/0967-0645(93)90072-U
915   Le Provost, C., Lyard, F., 1997. Energetics of the M2 barotropic ocean tides: an estimate
916   of bottom friction dissipation from a hydrodynamic model - ScienceDirect. Progress
917   in Oceanography 37–52.
918   Lellouche, J.-M., Greiner, E., Le Galloudec, O., Garric, G., Regnier, C., Drevillon, M.,
919   Benkiran, M., Testut, C.-E., Bourdalle-Badie, R., Gasparin, F., Hernandez, O., Levier,
920   B., Drillet, Y., Remy, E., Le Traon, P.-Y., 2018. Recent updates to the Copernicus
921   Marine Service global ocean monitoring and forecasting real-time 1⁄12° high-
922   resolution system. Ocean Science 14, 1093–1126. https://doi.org/10.5194/os-14-
923   1093-2018
924   Lentini, C.A.D., Magalhães, J.M., da Silva, J.C.B., Lorenzzetti, J.A., 2016. Transcritical
925   Flow and Generation of Internal Solitary Waves off the Amazon River: Synthetic
926   Aperture Radar Observations and Interpretation. Oceanography 29, 187–195.
927   Lentz, S.J., Limeburner, R., 1995. The Amazon River Plume during AMASSEDS: Spatial
928   characteristics and salinity variability. Journal of Geophysical Research: Oceans 100,
929   2355–2375. https://doi.org/10.1029/94JC01411
930   Li, C., Zhou, W., Jia, X., Wang, X., 2006. Decadal/interdecadal variations of the ocean
931   temperature and its impacts on climate. Adv. Atmos. Sci. 23, 964–981.
932   https://doi.org/10.1007/s00376-006-0964-7
933   Lyard, F.H., Allain, D.J., Cancet, M., Carrère, L., Picot, N., 2021. FES2014 global ocean
934   tide atlas: design and performance. Ocean Science 17, 615–649.
935   https://doi.org/10.5194/os-17-615-2021

936   Madec, G., Bourdallé-Badie, R., Chanut, J., Clementi, E., Coward, A., Ethé, C., Iovino,
937   D., Lea, D., Lévy, C., Lovato, T., Martin, N., Masson, S., Mocavero, S., Rousset, C.,
938   Storkey, D., Vancoppenolle, M., Müeller, S., Nurser, G., Bell, M., & Samson, G.,
939   (2019). NEMO ocean engine. In Notes du Pôle de modélisation de l'Institut Pierre-
940   Simon   Laplace   (IPSL)   (v4.0,   Number   27).   Zenodo.
941   https://doi.org/10.5281/zenodo.3878122

942   Madec, G. (2014), "NEMO ocean engine" (Draft edition r5171), *Note du Pôle de*
943   *modélisation 27*, Inst. Pierre-Simon Laplace, France, ISSN No 1288-1619.

944   Magalhaes, J.M., da Silva, J.C.B., Buijsman, M.C., Garcia, C. a. E., 2016. Effect of the
945   North Equatorial Counter Current on the generation and propagation of internal
946   solitary waves off the Amazon shelf (SAR observations). Ocean Science 12, 243–
947   255. https://doi.org/10.5194/os-12-243-2016

948   Mei, W., Xie, S.-P., Primeau, F., McWilliams, J.C., Pasquero, C., 2015. Northwestern
949   Pacific typhoon intensity controlled by changes in ocean temperatures. Science
950   Advances 1, e1500014. https://doi.org/10.1126/sciadv.1500014

951   Moisan, J.R., Niiler, P.P., 1998. The Seasonal Heat Budget of the North Pacific: Net Heat
952   Flux and Heat Storage Rates (1950–1990). Journal of Physical Oceanography 28,
953   401–421. https://doi.org/10.1175/1520-0485(1998)028<0401:TSHBOT>2.0.CO;2

954   Molinas, E., Carneiro, J.C., Vinzon, S., 2020. Internal tides as a major process in Amazon
955   continental shelf fine sediment transport. Marine Geology 430, 106360.
956   https://doi.org/10.1016/j.margeo.2020.106360

957   Muacho, S., da Silva, J.C.B., Brotas, V., Oliveira, P.B., 2013. Effect of internal waves on
958   near-surface chlorophyll concentration and primary production in the Nazaré Canyon
959   (west of the Iberian Peninsula). Deep Sea Research Part I: Oceanographic Research
960   Papers 81, 89–96. https://doi.org/10.1016/j.dsr.2013.07.012

961   Muller-Karger, F.E., McClain, C.R., Richardson, P.L., 1988. The dispersal of the
962   Amazon's water. Nature 333, 56–59. https://doi.org/10.1038/333056a0

963   Munk, W., Wunsch, C., 1998. Abyssal recipes II: energetics of tidal and wind mixing.
964   Deep Sea Research Part I: Oceanographic Research Papers 45, 1977–2010.
965   https://doi.org/10.1016/S0967-0637(98)00070-3

966   Nagai, T., Hibiya, T., 2015. Internal tides and associated vertical mixing in the Indonesian
967   Archipelago. Journal of Geophysical Research : Oceans 120, 3373–3390.
968   https://doi.org/10.1002/2014JC010592

969 Neto, A.V.N., da Silva, A.C., 2014. Seawater temperature changes associated with the
970   North Brazil current dynamics. Ocean Dynamics 64, 13–27.
971   https://doi.org/10.1007/s10236-013-0667-4

972 Nittrouer, C.A., DeMaster, D.J., 1996. The Amazon shelf setting: tropical, energetic, and
973   influenced by a large river. Continental Shelf Research 16, 553–573.
974   https://doi.org/10.1016/0278-4343(95)00069-0

975 Niwa, Y., Hibiya, T., 2014. Generation of baroclinic tide energy in a global three-
976   dimensional numerical model with different spatial grid resolutions. Ocean Modelling
977   80, 59–73. https://doi.org/10.1016/j.ocemod.2014.05.003

978 Niwa, Y., Hibiya, T., 2011. Estimation of baroclinic tide energy available for deep ocean
979   mixing based on three-dimensional global numerical simulations. J Oceanogr 67,
980   493–502. https://doi.org/10.1007/s10872-011-0052-1

981 Nugroho, D., Koch-Larrouy, A., Gaspar, P., Lyard, F., Reffray, G., Tranchant, B., 2018.
982   Modelling explicit tides in the Indonesian seas: An important process for surface sea
983   water properties. Marine Pollution Bulletin, Special Issue: Indonesia seas
984   management 131, 7–18. https://doi.org/10.1016/j.marpolbul.2017.06.033

985 Peng, S., Liao, J., Wang, X., Liu, Z., Liu, Y., Zhu, Y., Li, B., Khokiattiwong, S., Yu, W.,
986   2021. Energetics Based Estimation of the Diapycnal Mixing Induced by Internal
987   Tides in the Andaman Sea. Journal of Geophysical Research: Oceans 126.
988   https://doi.org/10.1029/2020JC016521

989 Pomar, L., Morsilli, M., Hallock, P., Bádenas, B., 2012. Internal waves, an under-explored
990   source of turbulence events in the sedimentary record. Earth-Science Reviews 111,
991   56–81. https://doi.org/10.1016/j.earscirev.2011.12.005

992 Richardson, P.L., Hufford, G.E., Limeburner, R., Brown, W.S., 1994. North Brazil Current
993   retroflection eddies. Journal of Geophysical Research: Oceans 99, 5081–5093.
994   https://doi.org/10.1029/93JC03486

995 Rosenthal, Y., Boyle, E.A., Slowey, N., 1997. Temperature control on the incorporation
996   of magnesium, strontium, fluorine, and cadmium into benthic foraminiferal shells
997   from Little Bahama Bank: Prospects for thermocline paleoceanography. Geochimica
998   et Cosmochimica Acta 61, 3633–3643. https://doi.org/10.1016/S0016-
999   7037(97)00181-6

1000 Ruault, V., Jouanno, J., Durand, F., Chanut, J., Benshila, R., 2020. Role of the Tide on the
1001   Structure of the Amazon Plume: A Numerical Modeling Approach. Journal of

1002   Geophysical   Research: Oceans   125,   e2019JC015495.
1003   https://doi.org/10.1029/2019JC015495

1004   Salamena, G.G., Whinney, J.C., Heron, S.F., Ridd, P.V., 2021. Internal tidal waves and
1005   deep-water renewal in a tropical fjord: Lessons from Ambon Bay, eastern Indonesia.
1006   Estuarine,   Coastal   and   Shelf   Science   253,   107291.
1007   https://doi.org/10.1016/j.ecss.2021.107291

1008   Schott, F.A., Dengler, M., Brandt, P., Affler, K., Fischer, J., Bourlès, B., Gouriou, Y.,
1009   Molinari, R.L., Rhein, M., 2003. The zonal currents and transports at 35°W in the
1010   tropical   Atlantic.   Geophysical   Research   Letters   30.
1011   https://doi.org/10.1029/2002GL016849

1012   Sharples, J., Tweddle, J.F., Green, J.A.M., Palmer, M.R., Kim, Y.-N., Hickman, A.E.,
1013   Holligan, P.M., Moore, C.M., Rippeth, T.P., Simpson, J.H., Krivtsov, V., 2007.
1014   Spring-neap modulation of internal tide mixing and vertical nitrate fluxes at a shelf
1015   edge   in   summer.   Limnology   and   Oceanography   52,   1735–1747.
1016   https://doi.org/10.4319/lo.2007.52.5.1735

1017   Shriver, J., Arbic, B., Richman, J., Ray, R., Metzger, E., Wallcraft, A., Timko, P., 2012.
1018   An evaluation of the barotropic and internal tides in a high-resolution global ocean
1019   circulation   model.   Journal   of   Geophysical   Research   117,   C10024.
1020   https://doi.org/10.1029/2012JC008170

1021   Smith, K.A., Rocheleau, G., Merrifield, M.A., Jaramillo, S., Pawlak, G., 2016.
1022   Temperature variability caused by internal tides in the coral reef ecosystem of
1023   Hanauma   bay,   Hawai'i.   Continental   Shelf   Research   116,   1–12.
1024   https://doi.org/10.1016/j.csr.2016.01.004

1025   Speer, K.G., Isemer, H.-J., Biastoch, A., 1995. Water mass formation from revised
1026   COADS data. Journal of Physical Oceanography 25, 2444–2457.

1027   Swift, J.H., Aagaard, K., 1981. Seasonal transitions and water mass formation in the
1028   Iceland and Greenland seas. Deep Sea Research Part A. Oceanographic Research
1029   Papers 28, 1107–1129. https://doi.org/10.1016/0198-0149(81)90050-9

1030   Tchilibou, M., Koch-Larrouy, A., Barbot, S., Lyard, F., Morel, Y., Jouanno, J., Morrow,
1031   R., 2022. Internal tides off the Amazon shelf during two contrasted seasons:
1032   interactions with background circulation and SSH imprints. Ocean Science 18, 1591–
1033   1618. https://doi.org/10.5194/os-18-1591-2022

1034   Tchilibou, M., Gourdeau, L., Lyard, F., Morrow, R., Koch Larrouy, A., Allain, D., Djath,
1035   B., 2020. Internal tides in the Solomon Sea in contrasted ENSO conditions. Ocean
1036   Science 16, 615–635. https://doi.org/10.5194/os-16-615-2020

1037   Tchilibou, M., Gourdeau, L., Morrow, R., Serazin, G., Djath, B., Lyard, F., 2018. Spectral
1038   signatures of the tropical Pacific dynamics from model and altimetry: a focus on the
1039   meso-/submesoscale   range.   Ocean   Science   14,   1283–1301.
1040   https://doi.org/10.5194/os-14-1283-2018

1041   Tuerena, R.E., Williams, R.G., Mahaffey, C., Vic, C., Green, J.A.M., Naveira-Garabato,
1042   A., Forryan, A., Sharples, J., 2019. Internal Tides Drive Nutrient Fluxes into the Deep
1043   Chlorophyll Maximum Over Mid-ocean Ridges. Global Biogeochemical Cycles 33,
1044   995–1009. https://doi.org/10.1029/2019GB006214

1045   Wallace, M.I., Meredith, M.P., Brandon, M.A., Sherwin, T.J., Dale, A., Clarke, A., 2008.
1046   On the characteristics of internal tides and coastal upwelling behaviour in Marguerite
1047   Bay, west Antarctic Peninsula. Deep Sea Research Part II: Topical Studies in
1048   Oceanography 55, 2023–2040. https://doi.org/10.1016/j.dsr2.2008.04.033

1049   Wang, X., Peng, S., Liu, Z., Huang, R.X., Qian, Y.-K, Li, Y., 2016. Tidal Mixing in the
1050   South China Sea: An Estimate Based on the Internal Tide Energetics. Journal of
1051   Physical Oceanography 46, 107–124. https://doi.org/10.1175/JPO-D-15-0082.1

1052   Wentz, F.J., C. Gentemann, K.A. Hilburn, 2015: Remote Sensing Systems TRMM TMI
1053   [indicate whether you used Daily, 3-Day, Weekly, or Monthly] Environmental Suite
1054   on 0.25 deg grid, Version 7.1, [indicate subset if used]. Remote Sensing Systems,
1055   Santa Rosa, CA. Available online at www.remss.com/missions/tmi.

1056   Xie, S.-P., Carton, J.A., 2004. Tropical Atlantic variability: Patterns, mechanisms, and
1057   impacts. Washington DC American Geophysical Union Geophysical Monograph
1058   Series 147, 121–142. https://doi.org/10.1029/147GM07

1059   Xu, P., Yang, W., Zhu, B., Wei, H., Zhao, L., Nie, H., 2020. Turbulent mixing and vertical
1060   nitrate flux induced by the semidiurnal internal tides in the southern Yellow Sea.
1061   Continental Shelf Research 208, 104240. https://doi.org/10.1016/j.csr.2020.104240

1062   Yadidya, B., Rao, A.D., 2022. Projected climate variability of internal waves in the
1063   Andaman Sea. Commun Earth Environ 3, 1–12. https://doi.org/10.1038/s43247-022-
1064   00574-8

1065 Zaron, E.D., 2019. Baroclinic Tidal Sea Level from Exact-Repeat Mission Altimetry.
1066   Journal of Physical Oceanography 49, 193–210. https://doi.org/10.1175/JPO-D-18-
1067   0127.1

1068 Zaron, E.D., 2017. Mapping the nonstationary internal tide with satellite altimetry. Journal
1069   of   Geophysical   Research: Oceans   122,   539–554.
1070   https://doi.org/10.1002/2016JC012487

1071 Zhao, Z., Alford, M.H., Girton, J.B., Rainville, L., Simmons, H.L., 2016. Global
1072   Observations of Open-Ocean Mode-1 M2 Internal Tides. Journal of Physical
1073   Oceanography 46, 1657–1684. https://doi.org/10.1175/JPO-D-15-0105.1

1074 Zhao, Z., Alford, M.H., Girton, J.B., 2012. Mapping Low-Mode Internal Tides from
1075   Multisatellite Altimetry. Oceanography 25, 42–51.

1076
1077
1078
1079
1080
1081
1082
1083
1084
1085
1086
1087
1088
1089
1090
1091
1092
1093
1094
1095
1096
1097
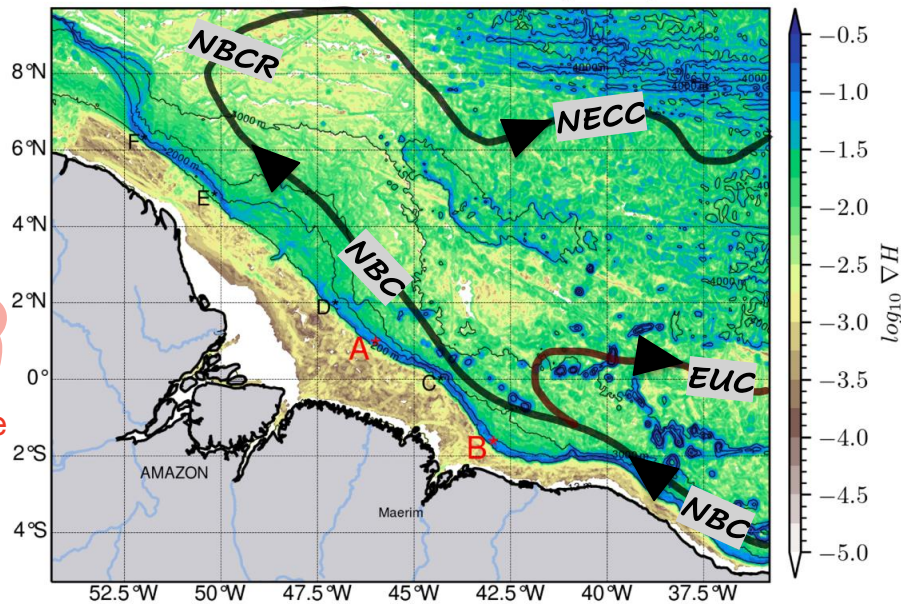
1098

Figure 1: The horizontal gradient (∇H) of the model's bathymetry with different internal tides generation sites (A*, B*, C*, D*, E* and F*) along the high slope (blue) of the shelf break, with the main sites (in red) being A* and B*, as mentioned in Magalhaes et al. (2016) and Tchilibou et al. (2022). Solid lines represent the circulation (as described by Didden and Schott, 1993; Richardson et al., 1994; Bourlès et al., 1999a; Johns et al., 1998; Schott et al., 2003; Garzoli et al., 2004) with NBC, NBCR and NECC pathways in black, and the EUC pathway in brown red. Tin black contours are 200 m, 2000 m, 3000 m and 4000 m isobaths.

1107

1108

1109

1110

1111

1112
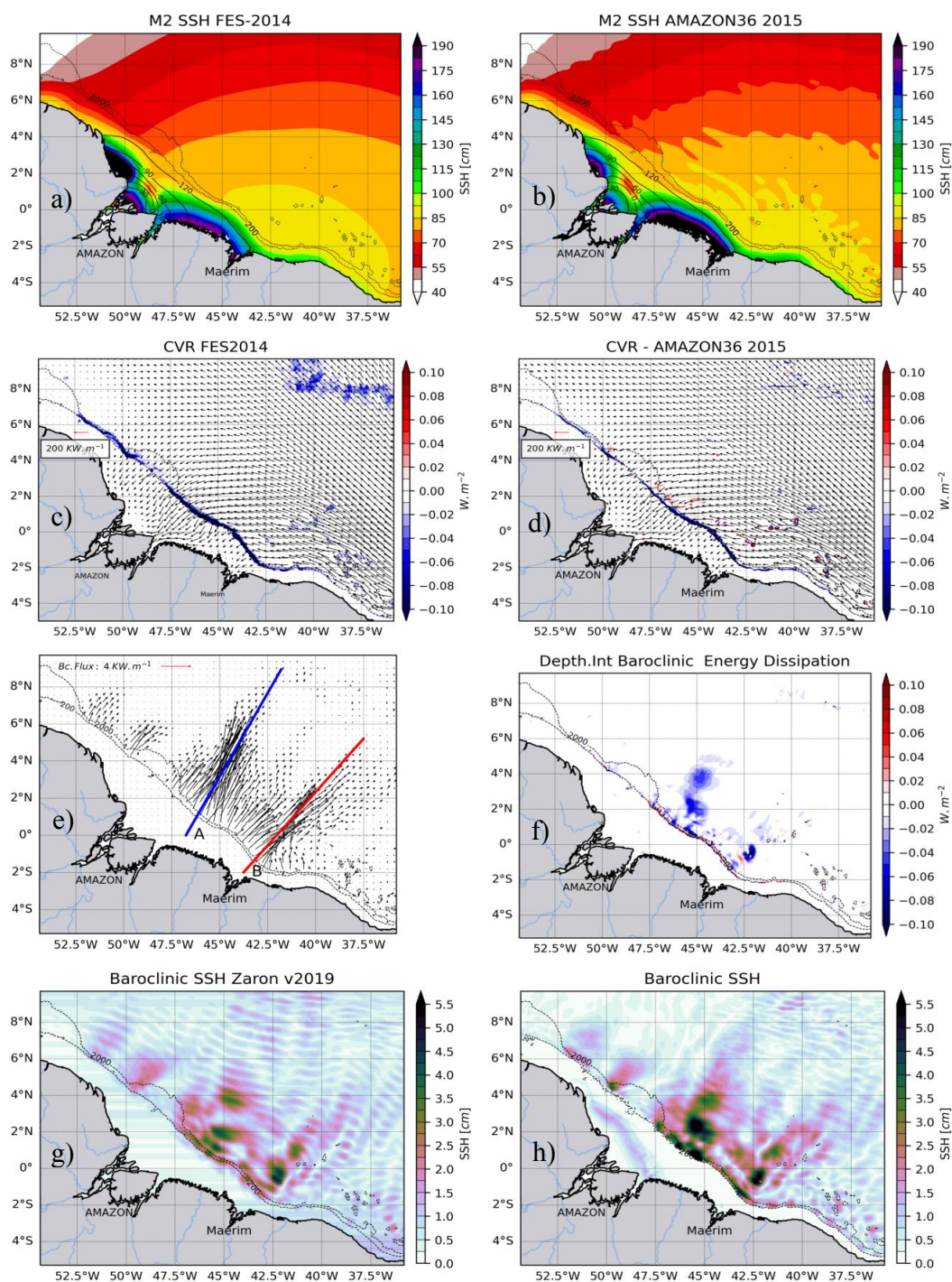
1114   *Figure 2: M2 tides (coherent) characteristics. Barotropic sea surface height for FES2014 (a)*

1115   *and model (b), depth-integrated energy conversion rate (CVR) (color shading) for FES2014*

1116   *(c) and model (d) with barotropic energy flux black arrows, model depth-integrated baroclinic*

1117   *energy flux black (e) arrows with transect lines along A (blue) and B (red) IT's pathways,*

1118   *model depth-integrated baroclinic energy dissipation (f), and baroclinic sea surface height*

1119   *from observation (Zaron, 2019) (g) and model (h).*

1120

1121

1122

1123

1124

1125

1126

1127

1128

1129

1130

1131

1132

1133

1134

1135
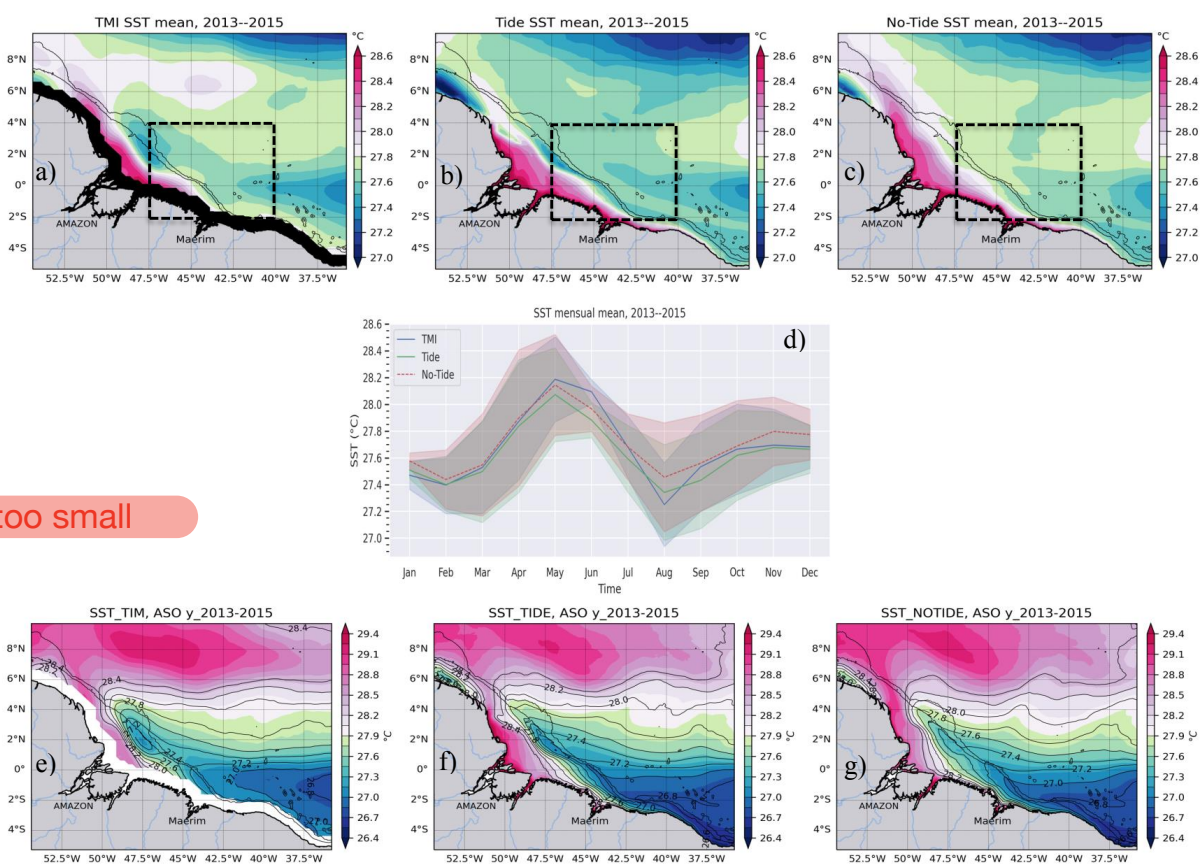
Fonts are too small

1136

1137   *Figure 3: Mean SST for the period 2013 to 2015 from TMI SST (a) with a black coastal mask,*

1138   *the model's tidal simulation (b), the model's non-tidal simulation (c), seasonal cycle of the SST*

1139   *of the three products averaged inside the dotted line box (covering IT pathways emanating*

1140   *from the main generation sites A and B) with shelf masked over the 200 m isobath, the bands*

1141   *give the variability according to standard deviation (d). The lower panels present the SST*

1142   *averaged for the ASO (August-September-October) season over the years 2013–2015 for TMI*

1143   *SST (e) with a white coastal mask, the model's tidal simulation (f) and the model's non-tidal*

1144   *simulation (g), with the white thin lines representing the temperature contours. The black tin*

1145   *lines stand for the 200 m and 2000 m isobaths.*

1146

1147

1148

1149

1150

1151

1152

1153

1154

1155

1156

1157

1158

1159

1160
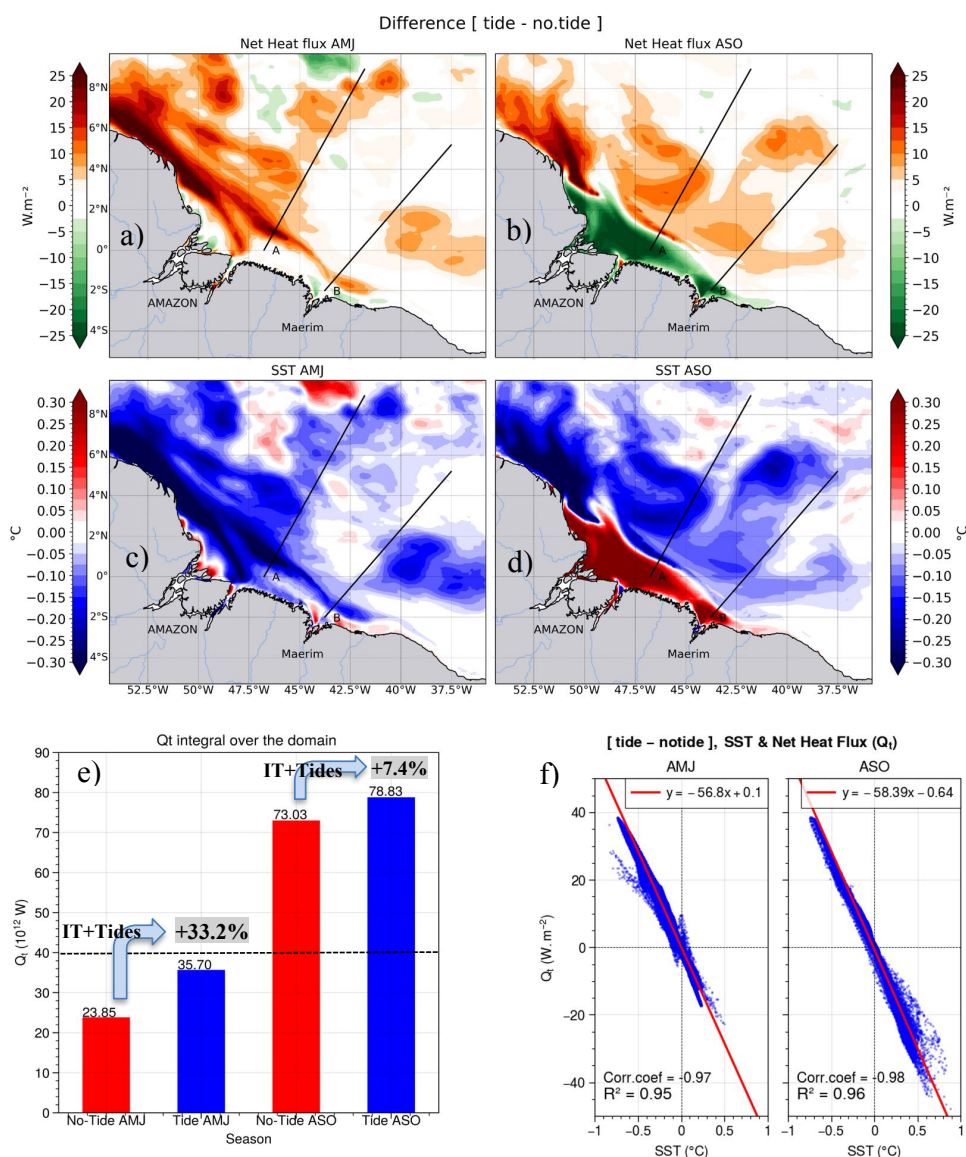
Figure 4: Relationship between the atmosphere-to-ocean net heat flux (Qt) and the SST: the Qt difference between tide and no-tide simulations in AMJ (a) and ASO (b) season, and SST difference in AMJ (c) and ASO (d), domain integrated Qt (e) for both seasons for each simulation. Correlation between Qt difference and SST difference for each season (f).

1169
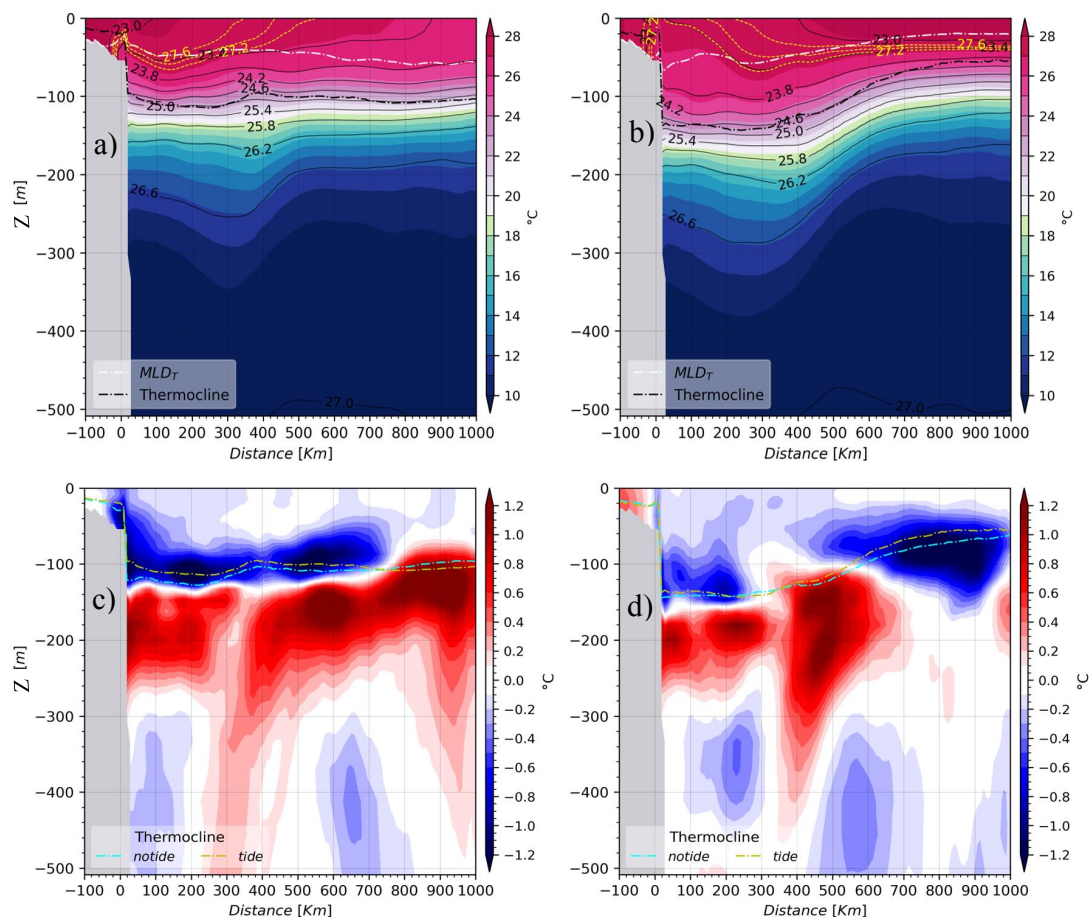
Figure 5: Vertical sections of tidal simulation's temperature following IT's pathway A for the AMJ (a) and ASO (b) seasons. Difference of temperature between tidal and non-tidal simulations for AMJ (c) and ASO (d) seasons. The yellow dotted and black tin lines in the upper panels are, respectively, for temperature and density anomaly isocontours, the black and white ticker dot-dashed lines are respectively thermocline and mixed layer depths. The yellow and cyan ticker dot-dashed lines in the lower panel are the thermocline depth respectively for tidal and non-tidal simulations.

1177

1178

1179

What's this???

Authors state earlier that paths A and B are similar, but they look very different here, especially in panel (b).
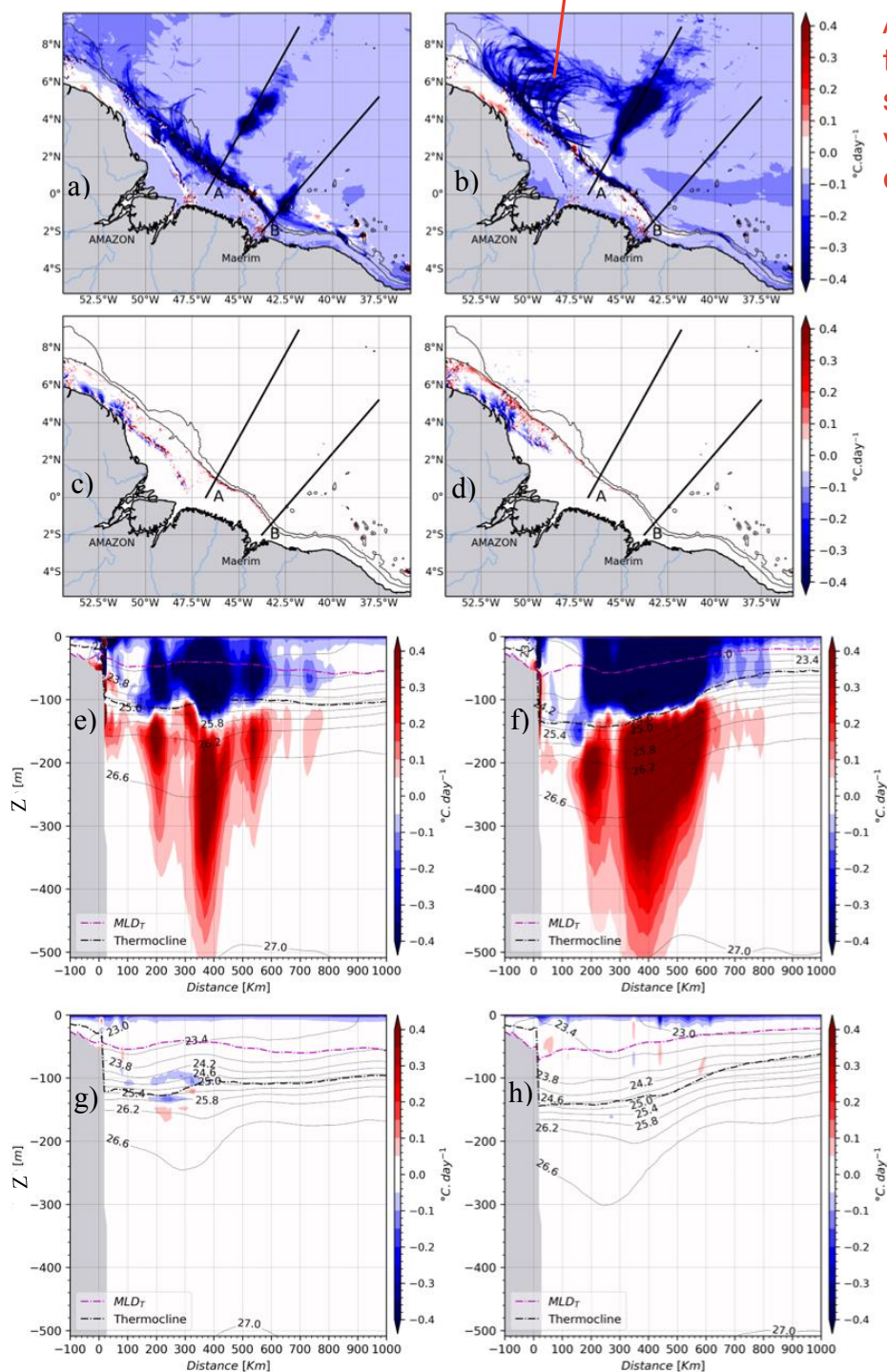
1180

1181   *Figure 6: The vertical diffusion of temperature (ZDF) for both seasons, respectively AMJ (left*

panel) and ASO (right panel). Vertical mean between 2–20 m for AMJ season in tidal (a) and non-tidal (c) simulation; then for ASO season in tidal (b) and non-tidal (d) simulations. Black thin contours are, from the coast to open ocean, 200 m and 2000 m isobaths. Vertical section following A for AMJ season in tidal (e) and non-tidal (g) simulations; then for ASO season in tidal (f) and no-tidal (h) simulation. The black and magenta ticker dot-dashed lines are respectively thermocline depth and mixed layer depth. Thin black contours are for density anomaly.
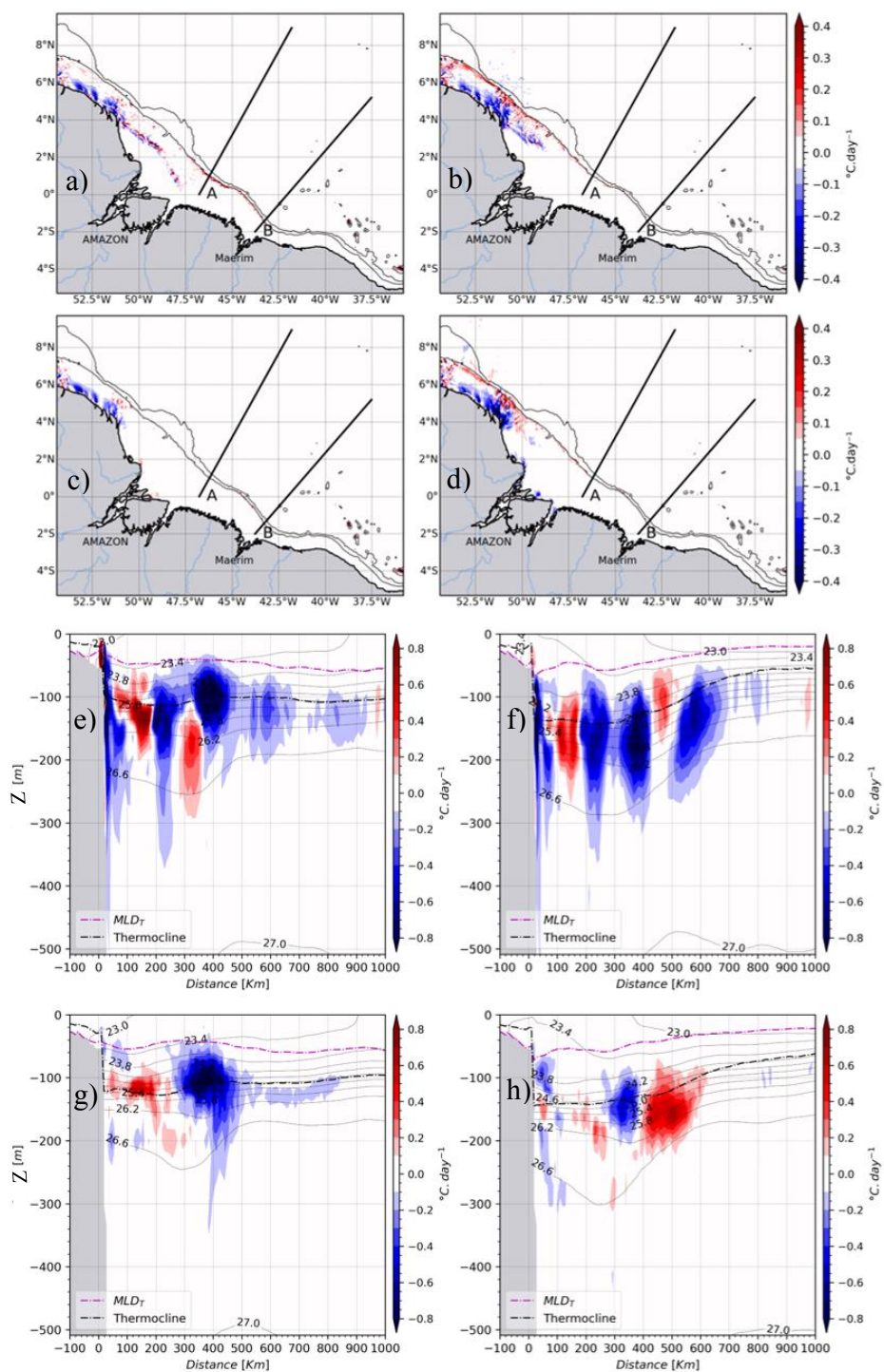
1204

1205   *Figure 7: same as figure 6, but for the vertical advection of temperature (z–ADV).*
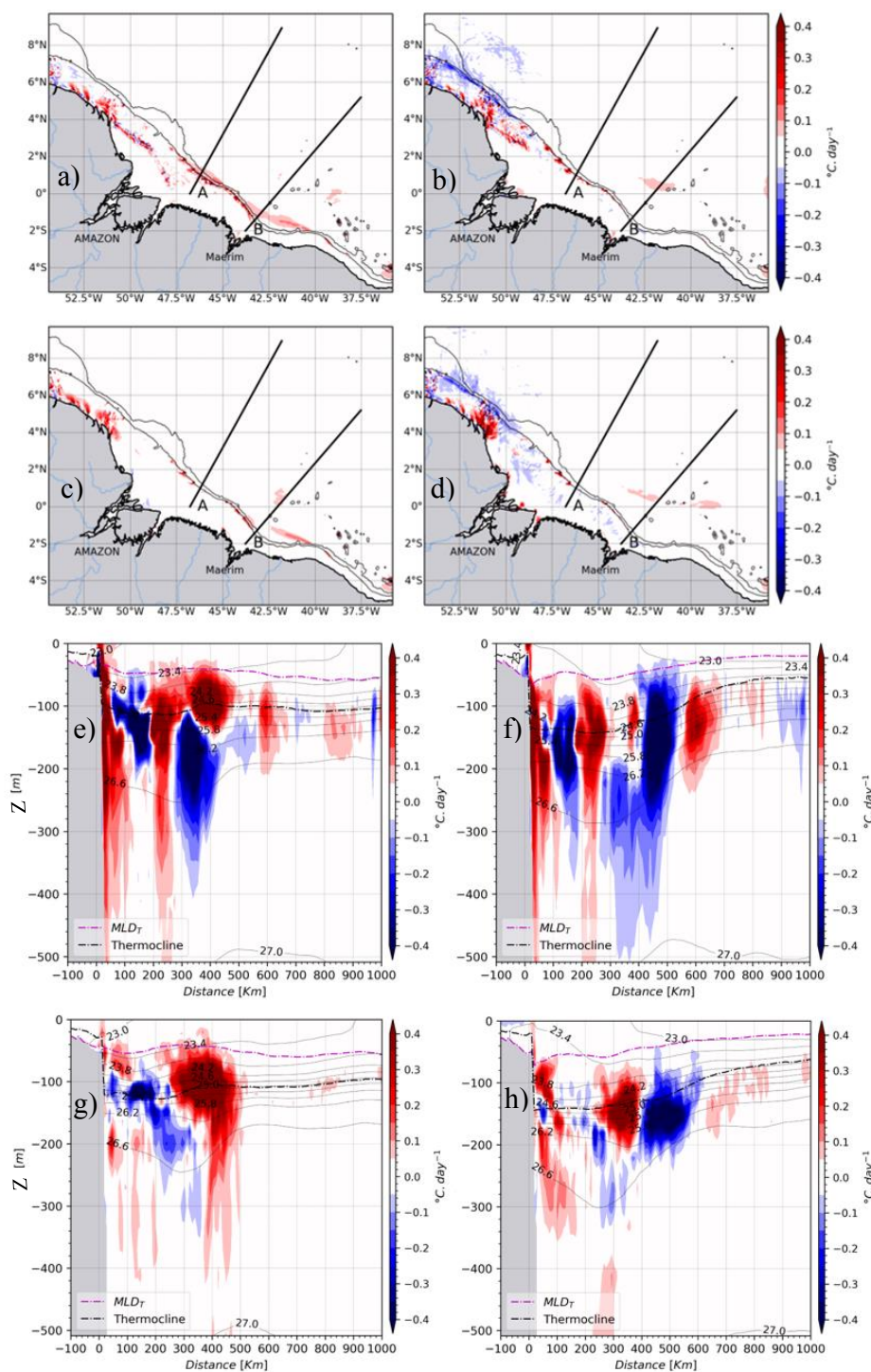
1206

Figure 8: same as figure 6 but for the horizontal advection of temperature (h-ADV = x–ADV

1207

1208   *+ y–ADV).*

1209

1210

1211

1212

1213

1214

1215

1216

1217

1218

1219

1220

1221

1222

1223

1224

1225

1226

1227

1228

1229

1230

1231

1232

1233

1234

1235

1236

1237

1238

1239

1240